J. Fluid Mech. (1993), vol. 256, pp. 647–683

Buoyancy-driven interactions between two deformable viscous drops

By MICHAEL MANGA[1] AND H. A. STONE[2]

[1]Department of Earth and Planetary Sciences, Harvard University, Cambridge, MA 02138, USA
[2]Division of Applied Sciences, Harvard University, Cambridge MA 02138, USA

(Received 11 March 1993)

Time-dependent interactions between two buoyancy-driven deformable drops are studied in the low Reynolds number flow limit for sufficiently large Bond numbers that the drops become significantly deformed. The first part of this paper considers the interaction and deformation of drops in axisymmetric configurations. Boundary integral calculations are presented for Bond numbers $\mathscr{B} = \Delta\rho g a^2/\sigma$ in the range $0.25 \leqslant \mathscr{B} < \infty$ and viscosity ratios λ in the range $0.2 \leqslant \lambda \leqslant 20$. Specifically, the case of a large drop following a smaller drop is considered, which typically leads to the smaller drop coating the larger drop for $\mathscr{B} \gg 1$. Three distinct drainage modes of the thin film of fluid between the drops characterize axisymmetric two-drop interactions: (i) rapid drainage for which the thinnest region of the film is on the axis of symmetry, (ii) uniform drainage for which the film has a nearly constant thickness, and (iii) dimple formation. The initial mode of film drainage is always rapid drainage. As the separation distance decreases, film flow may change to uniform drainage and eventually to dimpled drainage. Moderate Bond numbers, typically $\mathscr{B} = O(10)$ for $\lambda = O(1)$, enhance dimple formation compared to either much larger or smaller Bond numbers. The numerical calculations also illustrate the extent to which lubrication theory and analytical solutions in bipolar coordinates (which assume spherical drop shapes) are applicable to deformable drops.

The second part of this investigation considers the 'stability' of axisymmetric drop configurations. Laboratory experiments and two-dimensional boundary integral simulations are used to study the interactions between two horizontally offset drops. For sufficiently deformable drops, alignment occurs so that the small drop may still coat the large drop, whereas for large enough drop viscosities or high enough interfacial tension, the small drop will be swept around the larger drop. If the large drop is sufficiently deformable, the small drop may then be 'sucked' into the larger drop as it is being swept around the larger drop. In order to explain the alignment process, the shape and translation velocities of widely separated, nearly spherical drops are calculated using the method of reflections and a perturbation analysis for the deformed shapes. The perturbation analysis demonstrates explicitly that drops will tend to be aligned for $\mathscr{B} > O(d/a)$ where d is the separation distance between the drops.

1. Introduction

The low Reynolds number study of the buoyancy-driven interaction between a pair of drops or a drop and an interface serves as a useful model for understanding the dynamics of multiphase systems, e.g. liquid–liquid extraction which eventually requires the coalescence of a drop with its homophase, or the evolution of the dispersed phase volume fraction in multiphase flows common to industrial processing. Most previous studies of two-drop interactions assume spherical drop shapes, a limit which requires that interfacial tension forces are large compared to viscous and pressure forces. For example, the Stokes flow field around two translating spherical drops, as well as the rise speed and associated drag forces, have been examined theoretically using bipolar coordinates, the method of images, and the method of reflections (e.g. see references given by Barnocky & Davis 1989).

In this paper we consider the hydrodynamic interactions between two buoyant drops in a viscously dominated flow. Our contribution to the subject area is to investigate the case where buoyancy forces are much larger than the restoring forces due to interfacial tension, and hence large drop distortions are possible. First we use a boundary integral method to study numerically the on-axis interaction of two deformable translating drops. A related problem with hydrodynamic interactions between deformable drops was studied by Pozrikidis (1992*a*) in an investigation of a train of drops translating in a cylindrical tube. Second we consider experimentally and numerically the interaction of two buoyant, deformable drops which are not aligned vertically, and we develop simple far-field expressions describing the motion of a pair of deformable drops. For such off-axis configurations, the flow produced by the hydrodynamically interacting translating drops induces shape distortions that are responsible for the eventual on-axis rise of the two drops, leading to similar interactions characteristic of initially aligned drops.

Coalescence of two drops requires that the separation distance between the two drops eventually becomes very small; thus, the thin-film geometry and flow characteristic of the near contact between two drops has received much attention. Most studies make *ad hoc* approximations for some features of the thin-film flow geometry, though two recent studies obviate this deficiency. An approximate lubrication theory description of the two-drop geometry, valid for two nearly touching spherical drops, is presented by Davis, Schonberg & Rallison (1989) and Barnocky & Davis (1989). Yiantsios & Davis (1990, 1991) extend the lubrication approach to account for interface deformation in the limit that interfacial tension is sufficiently large to allow only small deformations; the evolution of drop shape as a function of viscosity ratio between the two fluids is determined and the formation of a dimpled shape is demonstrated without any *ad hoc* approximations other than assuming the validity of the lubrication approximation. The finite deformation and associated film drainage of a drop approaching a deformable fluid–fluid interface, in particular the effects of viscosity contrasts and interfacial tension, is addressed by Chi & Leal (1989) using a boundary integral method. The studies of Yiantsios & Davis and Chi & Leal thus describe the complete time evolution of an isolated drop interacting with a deformable boundary, at least for cases where only modest drop deformation occurs.

In the limit of low interfacial tension, drops may become highly deformed even when separation distances are large. Large shape distortions lead to a number of different types of two-drop interactions at low Reynolds numbers. The flows are characterized by large values of the Bond number, $\mathscr{B} = \Delta\rho g a_1^2/\sigma$, which represents the ratio of buoyancy forces to interfacial tension forces: $\Delta\rho$ is the density difference between the drop and surrounding fluid, g is the gravitational acceleration, a_1 is the radius of the larger of the two drops, and σ is the interfacial tension. In figure 1 we show the interaction that results from two air bubbles translating along their line-of-centres in a large container of corn syrup. The Bond number for this experiment is

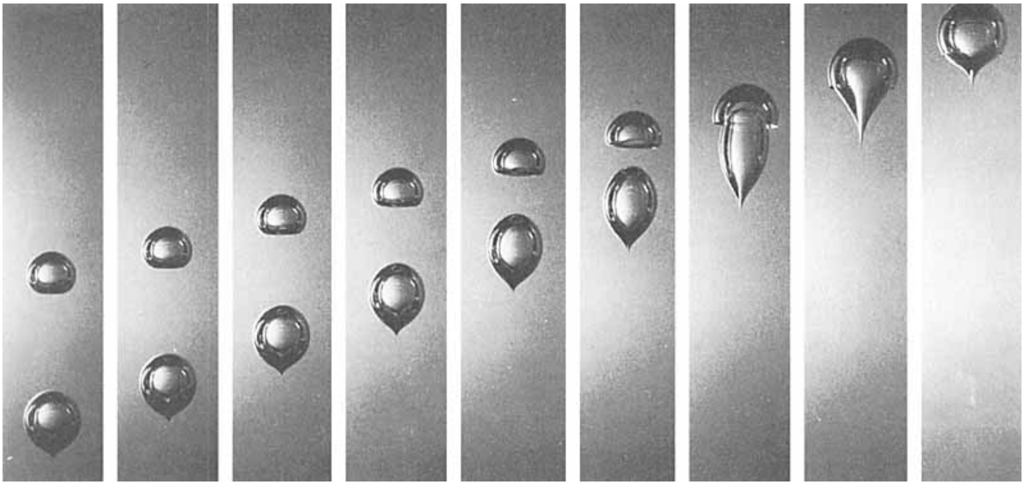

FIGURE 1. Sequence of photographs of air bubbles in corn syrup. The Bond number based on the larger drop is $\mathscr{B} \approx 100$ and the Reynolds number is $\mathscr{R} \approx 10^{-2}$. Photographs are shown at 5 s intervals. The trailing bubble has a small tail which develops as the bubble breaks off from the injection tube; at the time of break-off the tail is about one bubble radius long. Owing to the large viscosity of corn syrup, the tail does not completely relax before the first photograph is taken. In the experiments, coalescence occurs about 10 s after the final photograph shown.

large, $\mathscr{B} \approx 100$, and the Reynolds number based on the bubble radius a_1 and rise speed U is small, $\mathscr{R} = \rho U a_1/\mu \approx 10^{-2}$. This series of photographs illustrates that deformation may be large even when separation distances are large, and that the spherical-drop assumption commonly used to study drop interactions is not always a reasonable approximation. In the experiment, coalescence occurs shortly after the final photograph.

We note here that for situations where the interfacial tension forces are weak, such as the experiment illustrated in figure 1, the flow field created by the trailing drop (radius a_1) will tend to flatten the leading drop into an oblate shape. The velocity difference thus generated across the leading drop (radius a_2) is approximately $\Delta u \approx a_2 U_1/d$ for large separation distances d in a viscously dominated flow where U_1 is the speed of the trailing drop. Consequently, neglecting interfacial tension, the total strain or deformation experienced by the leading drop is $\tau \Delta u/a_2$, where τ is a characteristic time for the deformation to occur. Choosing $\tau = a_1/U_1$, which is the advective timescale characteristic of interaction of the two drops, gives a strain a_1/d experienced by the leading drop as a consequence of motion of the trailing drop. Thus, for separation distances of 4 drop radii, we can expect strains of 25%, or aspect ratios of about 3/2. We will see that even such modest shape distortions are important when considering the interaction of two drops which are not aligned initially along the vertical direction.

The two-drop interaction shown in figure 1, characterized by large distortions owing to large Bond numbers, is the primary focus of this paper. In §3 we use the boundary integral method to study axisymmetric two-drop configurations. In §4, we show experimental results typical of the interaction of initially offset drops and study a model for this off-axis configuration using a two-dimensional boundary integral formulation. Finally, in §5 we develop simple analytical results for the far-field, interaction-induced deformation and translational velocities using the method of reflections and the Reciprocal theorem in the limit of small shape distortions.

The spherical shape assumption is justified in many chemical engineering systems involving aqueous media so long as the drop radii are smaller than $O(10\,\mu\mathrm{m})$. Larger drops may be characterized by Bond numbers greater than $O(1)$ and significant deformation should be expected. We note that the study here is also relevant to a number of geological and geophysical problems where the Reynolds number is small because of high viscosities and the Bond number is large because of large lengthscales. At the longest lengthscales the behaviour of mantle plumes and diapirs, with lengthscales ranging from 10 km to 1000 km, can be modelled as buoyancy-driven drops (Manga, Stone & O'Connell 1993; Koch 1993). At smaller lengthscales, bubbles in high-viscosity silicate magmas, with typical radii of 1 mm to 1 cm, have Bond numbers greater than $O(1)$. Large Bond numbers may also be achieved owing to the presence of surfactants which may substantially decrease interfacial tension, though surfactants also induce motion because of gradients of interfacial tension. Such Marangoni motions are outside the scope of this investigation.

2. Problem formulation

The interaction of drops translating parallel to their line-of-centres is modelled by considering three fluid domains, the ambient fluid and the two drops, as shown in figure 2. To reduce the number of parameters we assume that the drops are composed of the same fluid, which corresponds to the most common problems of physical interest. The boundary integral method is used to numerically study this flow problem. The technique is well-established and has been used, for example, to study drop deformation in extensional flows (Rallison & Acrivos 1978) and the buoyancy-driven motion and stability of translating drops (Koh & Leal 1989; Pozrikidis 1990). Here we summarize for completeness the basic equations.

In the low Reynolds number limit the flow in each fluid domain satisfies the Stokes and continuity equations

$$\nabla \cdot \boldsymbol{T} = \mu \nabla^2 \boldsymbol{u} - \nabla p + \rho \boldsymbol{g} = 0 \quad \text{and} \quad \nabla \cdot \boldsymbol{u} = 0, \tag{2.1}$$

where $\boldsymbol{u}$ is the fluid velocity, p is the fluid pressure, $\boldsymbol{T}$ is the stress tensor defined to incorporate the body force $\rho \boldsymbol{g}$, i.e. $\boldsymbol{T} = -p\boldsymbol{I} + \mu[\nabla \boldsymbol{u} + (\nabla \boldsymbol{u})^T] + \rho \boldsymbol{g} \cdot \boldsymbol{x}\boldsymbol{I}$, and μ is the fluid viscosity. As the stress tensor $\boldsymbol{T}$ is defined to be divergence free, the body force thus appears in the boundary conditions, equations (2.4) and (2.5) below. We denote the fluid domains by subscripts 1 and 2 for drops 1 and 2, respectively, and by the subscript *ext* for the external fluid.

We require that the velocity decays to zero far from the drops,

$$\boldsymbol{u}_{ext} \to 0 \text{ as } |\boldsymbol{x}| \to \infty \tag{2.2}$$

and that the velocity is continuous across all interfaces,

$$\boldsymbol{u}_1 = \boldsymbol{u}_{ext} \text{ on } S_I \quad \text{and} \quad \boldsymbol{u}_2 = \boldsymbol{u}_{ext} \text{ on } S_{II}, \tag{2.3}$$

where S_I is the surface bounding drop 1, and S_{II} is the surface bounding drop 2. The stress jump $[\![\boldsymbol{n} \cdot \boldsymbol{T}]\!]$ across an interface is balanced by the density contrast and interfacial tension forces, which depend on the local curvature $\nabla_s \cdot \boldsymbol{n}$ of the interface:

$$[\![\boldsymbol{n} \cdot \boldsymbol{T}^I]\!] = \boldsymbol{n} \cdot \boldsymbol{T}^I_{ext} - \boldsymbol{n} \cdot \boldsymbol{T}^I_1 = \sigma\,(\nabla_s \cdot \boldsymbol{n})\boldsymbol{n} + \boldsymbol{n}\Delta\rho\,(\boldsymbol{g} \cdot \boldsymbol{x}) \quad \text{on } S_I, \tag{2.4}$$

$$[\![\boldsymbol{n} \cdot \boldsymbol{T}^{II}]\!] = \boldsymbol{n} \cdot \boldsymbol{T}^{II}_{ext} - \boldsymbol{n} \cdot \boldsymbol{T}^{II}_2 = \sigma\,(\nabla_s \cdot \boldsymbol{n})\boldsymbol{n} + \boldsymbol{n}\Delta\rho\,(\boldsymbol{g} \cdot \boldsymbol{x}) \quad \text{on } S_{II}, \tag{2.5}$$

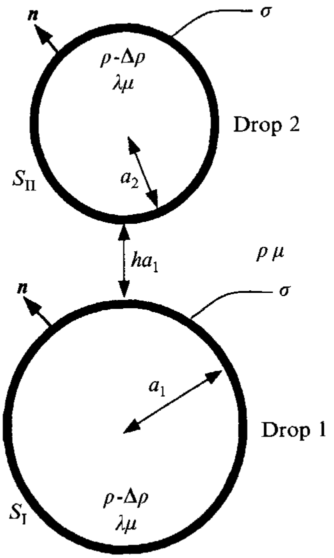

FIGURE 2. Geometry of the problem considered in § 3. The unit normal vector $\boldsymbol{n}$ is directed outward from the drops. Drops 1 and 2 have radii a_1 and a_2, respectively. The drops have viscosity $\lambda\mu$ and density $\rho - \Delta\rho$; the external fluid has viscosity μ and density ρ. The interfacial tension is denoted by σ. The separation distance between the drops is ha_1. The surfaces of the drops are denoted by S_I and S_{II}.

where σ denotes the constant interfacial tension, $\boldsymbol{n}$ is the unit normal directed into the external fluid, and $\nabla_s = (\boldsymbol{I} - \boldsymbol{nn}) \cdot \nabla$ is the gradient operator tangent to the interface. Additionally there is a kinematic constraint, which requires that a fluid element on a fluid–fluid interface remain on that interface for all time; formally, the kinematic constraint may be expressed with the Lagrangian description

$$\frac{\mathrm{d}\boldsymbol{x}_s}{\mathrm{d}t} = \boldsymbol{u}_s \quad \text{on } S_I \text{ and } S_{II}. \tag{2.6}$$

For convenience, the trailing drop is labelled drop 1, and the leading drop is labelled drop 2. The equations are non-dimensionalized by choosing the characteristic length as the radius of the trailing drop, radius a_1, the velocity scale as $\Delta\rho g a_1^2/\mu$, and an advective time-scale of $\mu/\Delta\rho g a_1$. For a given initial configuration (dimensionless separation distance h in figure 2), three dimensionless parameters characterize the flow: the ratio of drop radii, a_1/a_2, the viscosity ratio, λ, and a Bond number based on the properties of the trailing drop

$$\mathscr{B} = \frac{\Delta\rho g a_1^2}{\sigma}. \tag{2.7}$$

The Bond number characterizing the deformation of drop 2 with radius a_2 is $\mathscr{B}(a_2/a_1)^2$. In this paper we will assume that the drops are of comparable sizes, and often use a to denote a typical drop radius.

We solve for the time-dependent deformation and translation of the drops by recasting the Stokes equations as a pair of coupled integral equations of the second kind for the interfacial velocities. The integral equations involve only stress jumps (equations (2.4) and (2.5)) across the interfaces and the unknown velocities along the interfaces, $\boldsymbol{u}_I$ and $\boldsymbol{u}_{II}$, and are given by (see Appendix A for a derivation of the boundary integral equations for generic two-interface problems)

$$
\begin{aligned}
&-\frac{2}{1+\lambda}\int_{S_I}\left[\frac{1}{\mathscr{B}}\nabla_s\cdot\boldsymbol{n}-\hat{\boldsymbol{g}}\cdot\boldsymbol{y}\right]\boldsymbol{n}\cdot\boldsymbol{J}\mathrm{d}S_y \;-\; \frac{2(1-\lambda)}{1+\lambda}\int_{S_I}\boldsymbol{n}\cdot\ \boldsymbol{K}\cdot\boldsymbol{u}_I\mathrm{d}S_y\\
&-\frac{2}{1+\lambda}\int_{S_{II}}\left[\left(\frac{a_1}{a_2}\right)^2\frac{1}{\mathscr{B}}\nabla_s\cdot\boldsymbol{n}-\hat{\boldsymbol{g}}\cdot\boldsymbol{y}\right]\boldsymbol{n}\cdot\boldsymbol{J}\mathrm{d}S_y\\
&-\frac{2(1-\lambda)}{1+\lambda}\int_{S_{II}}\boldsymbol{n}\cdot\boldsymbol{K}\cdot\boldsymbol{u}_{II}\mathrm{d}S_y=\begin{cases}\boldsymbol{u}_I(\boldsymbol{x}), & \boldsymbol{x}\in S_I\\ \boldsymbol{u}_{II}(\boldsymbol{x}), & \boldsymbol{x}\in S_{II},\end{cases}
\end{aligned}
\tag{2.8}
$$

where $\boldsymbol{J}$ and $\boldsymbol{K}$ are known kernels for velocity and stress, respectively (Pozrikidis 1992*b*), $\hat{\boldsymbol{g}}$ is a unit vector in the direction of gravity, and y is the integration variable. The interfacial velocities $\boldsymbol{u}_I$ and $\boldsymbol{u}_{II}$ are determined by solving equation (2.8) and the time-dependent motion of the interface is determined using the kinematic condition (2.6). The numerical procedure for solving (2.8) is straightforward and is similar to the method outlined in Stone & Leal (1989). For the axisymmetric configuration studied in § 3, azimuthal integration may be performed analytically (Lee & Leal 1982) reducing (2.8) to a line integral. The integral equation is solved by a collocation procedure and integration is performed using Gauss–Legendre quadrature. The interface shapes are described by taut cubic splines (de Boor 1978) parameterized in terms of arclength. Typically, we use 50–90 collocation points on each half-interface. For a more complete discussion of boundary integral methods as applied to free-boundary problems the reader is referred to Pozrikidis (1992*b*) and Tanzosh, Manga & Stone (1992).

Cumulative numerical error, estimated by monitoring the volume change of the drops, may occasionally be as high as 5–10% for the most severe distortions and the times of the longest numerical simulations, particularly for problems involving large viscosity contrasts. Such volume changes are larger than those reported in previous studies because of the large distances over which the drops translate in the simulations. Typically, calculated interfacial velocities for a single spherical drop in an unbounded fluid differ by less than 1% from the exact Hadamard–Rybczyński result. In the results presented here, the volume changes were always less than 10% and no volume rescaling was implemented.

3. On-axis interaction of axisymmetric drops

The numerical results presented below illustrate the interaction between two axisymmetric drops translating along their line-of-centres. Qualitatively, the numerical results have some similarities with the problem of a drop approaching a deformable interface (Chi & Leal 1989). Most notably, the style of film drainage between the two drops is similar to the film formed between a drop and a fluid–fluid interface, though we allow for large interface distortions since the zero interfacial tension limit is studied.

We consider the case of a large drop following a smaller drop so that interaction eventually occurs; the two drops are composed of the same fluid and the radius ratio $a_1/a_2 = 2$ in all the simulations. Thus, the Bond number for the smaller drop is $0.25\mathscr{B}$. Both drops are assumed to be initially spherical and the initial separation distance between the two drops (the distance h shown in figure 2) is usually chosen as one half the radius of the large drop. Changing the ratio of drop sizes and the initial drop separation distance results in only modest qualitative changes in drop

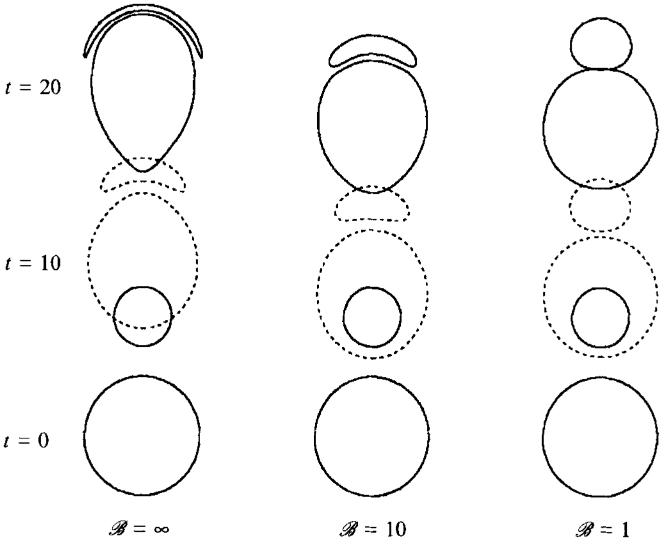

FIGURE 3. Effect of interfacial tension on drop deformation; $\mathscr{B} = \infty$, 10, 1; $\lambda = 1$; $a_1/a_2 = 2$. Interface shapes are shown at times $t = 0$, 10 and 20.

behaviour. However, the history of deformation is important for understanding the detailed drop deformation in the high Bond number limit owing to the long-range nature of Stokes flows; in § 3.4 we summarize typical results observed when the initial separation distance is changed.

3.1. *Effect of interfacial tension*

In figure 3 we illustrate the effect of interfacial tension on the shapes of translating drops. A sequence of interface shapes at equal time increments is shown for Bond numbers $\mathscr{B} = \infty$, 10 and 1. For all Bond numbers the smaller leading drop initially deforms into an oblate shape and the larger trailing drop deforms into a prolate shape; both types of deformation are a result of the flow produced by the neighbouring drop. For example, as schematically indicated in figure 4 using the simple idealization of treating the translating drop as a point force, the trailing drop becomes elongated (prolate distortion) owing to the viscous stresses associated with the convergence of streamlines in the flow produced by the leading drop; conversely, the leading drop becomes flattened (oblate distortion) owing to the viscous stresses associated with the divergence of streamlines in the flow produced by the trailing drop (analytical descriptions of the non-spherical shapes are given in § 5).

For translational motions in an unbounded fluid the spherical drop shape is stable to infinitesimal perturbations provided the interfacial tension is finite, i.e. $\mathscr{B} < \infty$ (Kojima, Hinch & Acrivos 1984). However, finitely deformed drop shapes are unstable, and subsequently undergo a continual deformation, if the restoring interfacial tension forces are not sufficiently large: prolate drops will develop long tails and oblate drops will develop cavities (Koh & Leal 1989; Pozrikidis 1990). For the isoviscous drops shown in figure 3, Bond numbers of order 10 appear to be sufficient to prevent the large drop from developing a tail (see figure 6 for shapes at longer times). As the restoring interfacial tension force is reduced, the smaller leading drop deforms substantially, spreading over the surface and thus coating the larger drop, as illustrated for the $\mathscr{B} = \infty$ and $\mathscr{B} = 10$ simulations. At longer times, the separating film thins

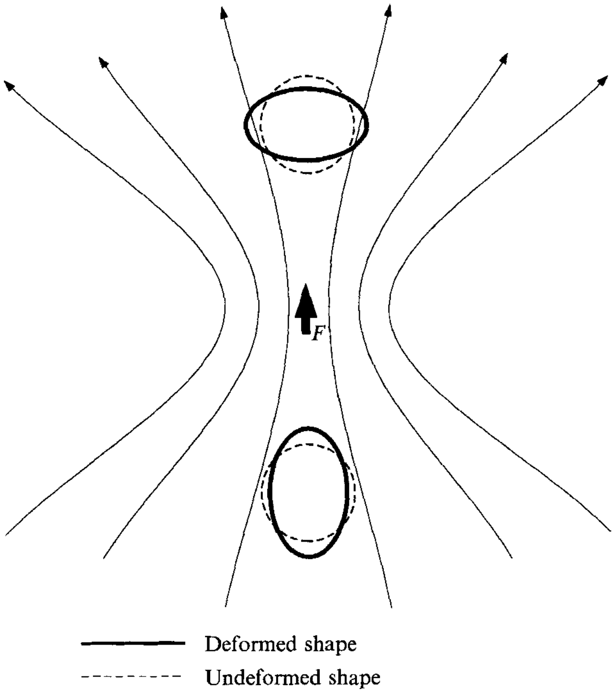

FIGURE 4. Illustration of the effect of a point force on drop deformation. Drops in front of a point force, which models the presence of a second drop, have oblate spheroidal shapes. Conversely, drops behind a point force have prolate spheroidal shapes.

substantially, the drops numerically make contact, and the simulation is terminated. The same manner of interaction and deformation was shown previously for the two air bubbles translating through corn syrup (figure 1).

3.2. *The style of film drainage*

The interaction over long times and possible coalescence of two nearly touching drops is controlled by the dynamics of the thin film between the drops. Interest in the coalescence process has been the primary motivation for the extensive study of the film drainage problem; the use of a boundary integral method allows us to study the complete evolution of the thin film for large drop deformations. When the interfaces are deformable, three distinct modes of film drainage characterize the interaction of two drops, analogous to the three modes described by Chi & Leal (1989) for a drop approaching its initially planar homophase. The three styles of interface deformation, which provide insight into the probable manner and location of coalescence, are referred to as (i) rapid drainage, (ii) uniform drainage and (iii) dimple formation, depending on the thickness profile of the film and the manner in which the film thins.

Numerical simulations illustrating the three modes of film flow are presented in figure 5. The film profiles (gap thickness as a function of radial position) are also shown. We note that 'uniform drainage' characterizes an almost (but not exact) uniform film thickness between two drops.

The three modes of film drainage also characterize different stages in the evolution of a given film. As we will see in the following sections, as the separation between the drops decreases, the characterization of the drainage flow may change from rapid

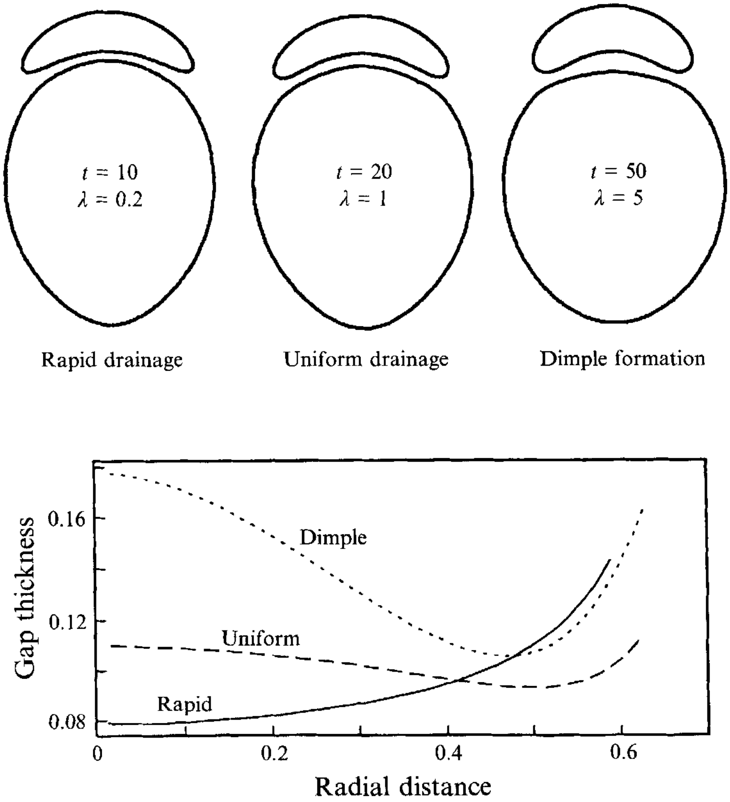

FIGURE 5. The three modes of film drainage, analogous to the three modes described in Chi & Leal (1989): (i) rapid drainage, (ii) uniform drainage, and (iii) dimple formation. Examples of calculated shapes for each mode are shown for $\mathscr{B} = 10$; $\lambda = 0.2$, 1 and 5; $a_1/a_2 = 2$. In the lower portion of the figure we plot gap thickness versus radial distance to illustrate more clearly the differences in gap geometry.

to uniform drainage and then dimple formation. For the range of viscosity ratios considered in this paper, the separation distance h at which dimple formation begins decreases with decreasing viscosity ratio λ for a given Bond number. In the studies by Yiantsios & Davis (1990, 1991), which are restricted to small Bond numbers, $\mathscr{B} \ll 1$, dimple formation is always predicted to eventually occur, provided attractive van der Waals forces are negligible. However, in our high Bond number calculations (e.g. $\mathscr{B} = \infty$ shown later in figure 6) and experiments with air bubbles (e.g. figure 1) dimple formation never appears to occur prior to coalescence. In the following section we discuss the effects of interfacial tension and drop viscosity on the style of drainage and outline the physical mechanisms responsible for the corresponding drainage mode.

3.3. *Rate of film drainage and dimple formation*

In figure 6 we present the time evolution of the gap thickness measured at $r = 0$, shown with a solid line, for different values of the Bond number and $\lambda = 1$. Corresponding drop shapes at different stages of the interaction are shown and identified with the letters a, b, c, etc. The minimum separation distance between the two drops is shown with a dashed line. Dimple formation in the thin film thus begins when the solid and dashed lines diverge indicating that the smallest separation distance is no longer

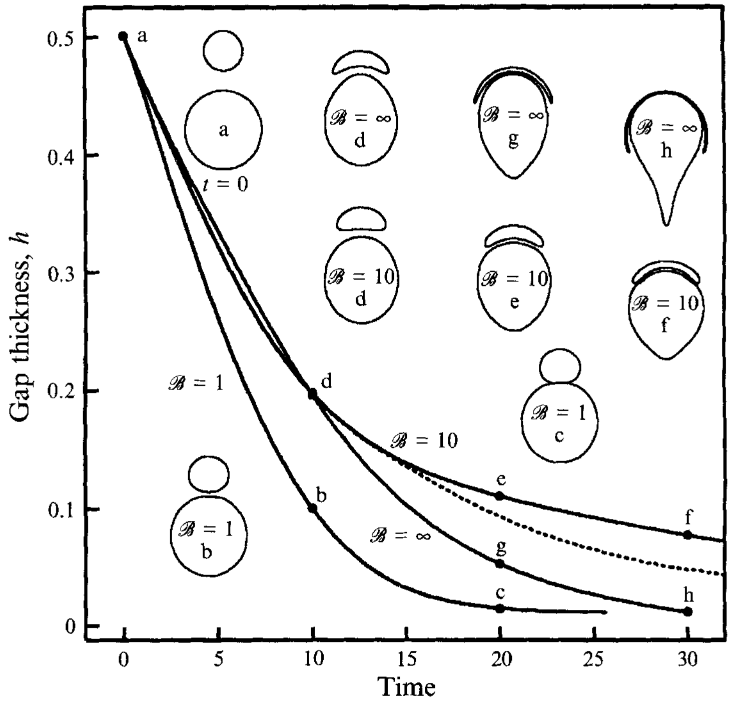

FIGURE 6. The rate of film drainage versus time for drops with Bond numbers $\mathscr{B} = 1$, 10 and ∞; $\lambda = 1$; $a_1/a_2 = 2$. The solid curve corresponds to the thickness of the film on the axis of symmetry, $r = 0$, and the dashed curve corresponds to the minimum film thickness. Drop shapes at different times are shown for reference.

along the centreline. The solid and dashed curves for $\mathscr{B} = 1$ and ∞ overlap since no dimple develops. The film thickness decreases most rapidly for the large interfacial tension simulation ($\mathscr{B} = 1$), and most slowly for the moderate interfacial tension simulation ($\mathscr{B} = 10$) which forms a dimpled film.

In order to explain the variation of film thickness with time, we note that for smaller Bond numbers (hence smaller distortions), film drainage is more rapid because the two drops remain nearly spherical and thus fluid in the gap is not forced to flow over too large a surface area. For the case of vanishing interfacial tension ($\mathscr{B} = \infty$), the smaller drop coats the larger drop, so that the increase in surface area provides additional resistance to fluid motion in the narrow gap which delays film thinning. Dimple formation for moderate Bond numbers ($\mathscr{B} = 10$; see also figure 5) means that the narrowest portion of the film is away from the centreline; this geometric constriction further slows the rate of film drainage. From the results shown in figure 6, we observe that in the absence of interfacial tension ($\mathscr{B} = \infty$) the thin film has a nearly uniform thickness over the entire surface of near-contact and no dimpled film develops; hence, the rate of thinning is intermediate between the $\mathscr{B} = 1$ and $\mathscr{B} = 10$ simulations.

Varying the viscosity ratio also has a significant effect on the rate and manner of film drainage, as shown in figure 7 for the case of $\mathscr{B} = 10$. A dimpled film forms earliest for the isoviscous drops; for higher viscosity ratios, a dimple forms at larger drop separation distances. Nevertheless, if we instead choose to non-dimensionalize time so as to highlight the higher viscosity fluid, i.e. define dimensionless time such

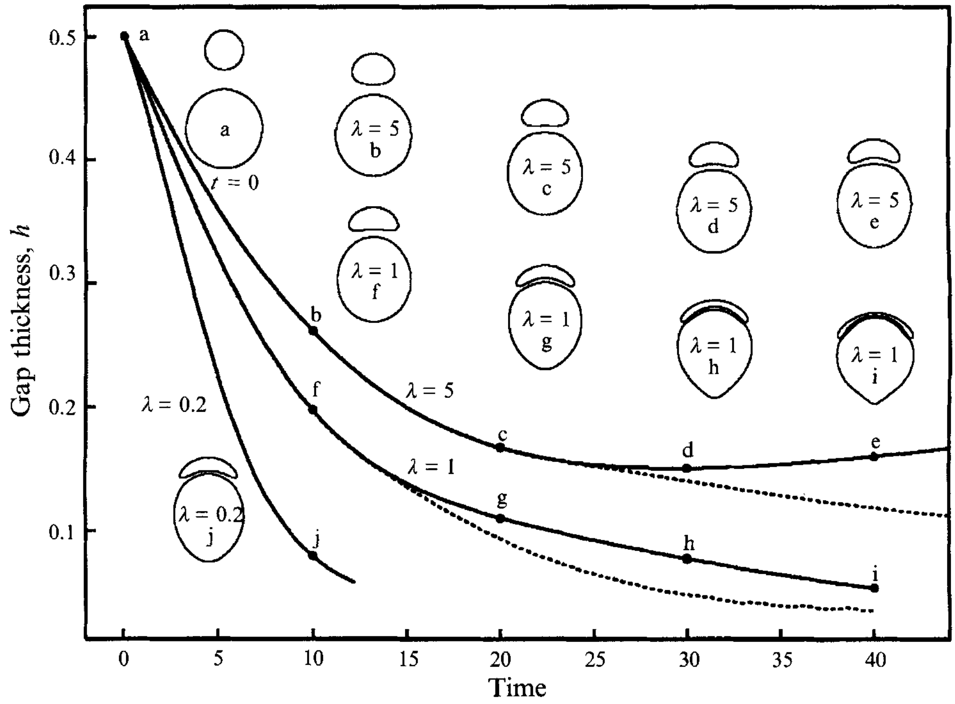

FIGURE 7. The rate of film drainage versus time for drops with viscosities $\lambda = 0.2$, 1 and 5; $\mathscr{B} = 10$; $a_1/a_2 = 2$. The solid curve corresponds to the thickness of the film on the axis of symmetry, $r = 0$, and the dashed curve corresponds to the minimum film thickness. Drop shapes at different times are shown for reference.

that $\bar{t} = t/(1+\lambda)$, then dimple formation actually occurs earlier for high-viscosity drops.

For low-viscosity drops, corresponding to a more mobile interface (Davis *et al.* 1989), the rate of film drainage is enhanced. For high-viscosity drops the interface becomes immobile, and not only offers additional resistance to fluid flow in the thin film, but also enhances the formation of dimples thus leading to a slower rate of drainage. We observe that in the higher viscosity ratio simulations, such as the case $\lambda = 5$ shown in figure 7, the gap thickness along the axis of symmetry actually increases after a certain stage in the development of a dimpled film. Since large pressures exist at $r = 0$ in order to squeeze fluid out of the thinning film, it becomes easier for the drop to distort such that the thickness of the gap increases at the film midpoint. This behaviour is associated with moderate values of the Bond number and is to be contrasted with the qualitatively different, monotonically thinning, low Bond number film profiles determined by Davis *et al.* (1989) and calculated by Chi & Leal (1989).

Although the thin film thickens along the axis of symmetry, the volume of fluid contained within the thin-film region continues to decrease with time. We also note that in the calculations of Yiantsios & Davis (1991), which incorporate van der Waals forces, the thickness of the gap increases once 'rim-rupture' begins.

For drops that remain nearly spherical (small Bond numbers), the radius of the dimple can be predicted by balancing the pressure in the film against the buoyancy force, giving a dimple radius of $r_d/a_1 = O(\mathscr{B}^{\frac{1}{2}})$ (e.g. Yiantsios & Davis 1991). In

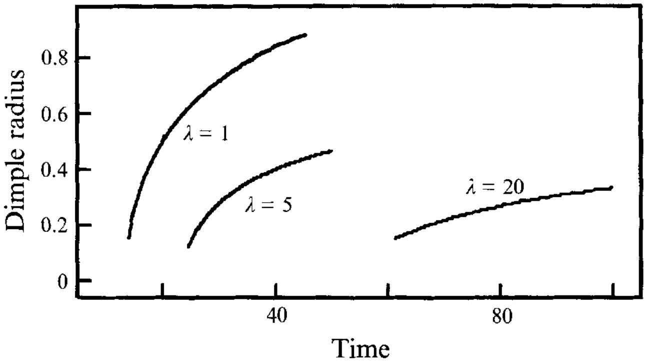

FIGURE 8. Dimple radius (normalized to a_1) as a function of time for viscosity ratios $\lambda = 1$, 5 and 20; $\mathscr{B} = 10$; $a_1/a_2 = 2$. The initial dimple radius is about $0.15a_1$ for all cases.

figure 8 we plot the dimple radius against time for the case of $\mathscr{B} = 10$ and $\lambda = 1$, 5 and 20. For all cases the initial dimple radius is about $0.15a_1$ and increases with time. The low Bond number estimate is not valid for these highly deformed drops since dimple radii greater than the drop radius are predicted. Predicting dimple radii for highly deformed drops is difficult since simple analytical approximations of drop shapes and pressure in the gap are not yet available.

3.4. *History effects*

For each of the above calculations we have assumed that the initial separation distance is $0.5a_1$. In figure 9 we show the rate of decrease of gap thickness $\mathrm{d}h/\mathrm{d}t$ for initial separation distances of $0.5a_1$ and $2.5a_1$ and different viscosity ratios. The Bond number is taken to be large enough, $\mathscr{B} = 10$, that large distortions are possible. The results in figure 9 demonstrate that for small dimensionless separation distances h the approach velocity $\mathrm{d}h/\mathrm{d}t$ is smaller at a given h for larger initial separations. If the initial separation distance is large ($2.5a_1$), the corresponding drop distortions are larger: larger initial separations provide more time for deformation.

From the numerical simulations, we observe that for the drop pairs with $\lambda = 1$ and 5, the dimple forms at larger separations h which leads to smaller rates of approach $\mathrm{d}h/\mathrm{d}t$ when two different initial conditions are compared at the same separation distance. For the case with $\lambda = 0.2$ dimples do not develop during the simulation. We note that although $\mathrm{d}h/\mathrm{d}t$ initially increases for $\lambda = 0.2$ for the small initial separation distance (because the large trailing drop becomes a prolate ellipsoid and is extended) the separation distance between the centre-of mass of the two drops decreases monotonically.

3.5. *Comparison with analytical results*

Here we consider the extent to which analytical results may be applied to describe the on-axis interaction of deformable drops. In figure 10 we show the rate of decrease of gap thickness $\mathrm{d}h/\mathrm{d}t$ as a function of the dimensionless separation distance h for (i) two numerical simulations ($\mathscr{B} = 1$ and 10; $\lambda = 1$) indicated by the solid curves, (ii) the results of a lubrication analysis indicated by a dotted line, and (iii) an exact solution for spherical drops in bipolar coordinates indicated by a dashed curve.

The lubrication analysis which combines lubrication theory and boundary integral methods (Barnocky & Davis 1989; Davis *et al.* 1989) is applicable to spherical shapes

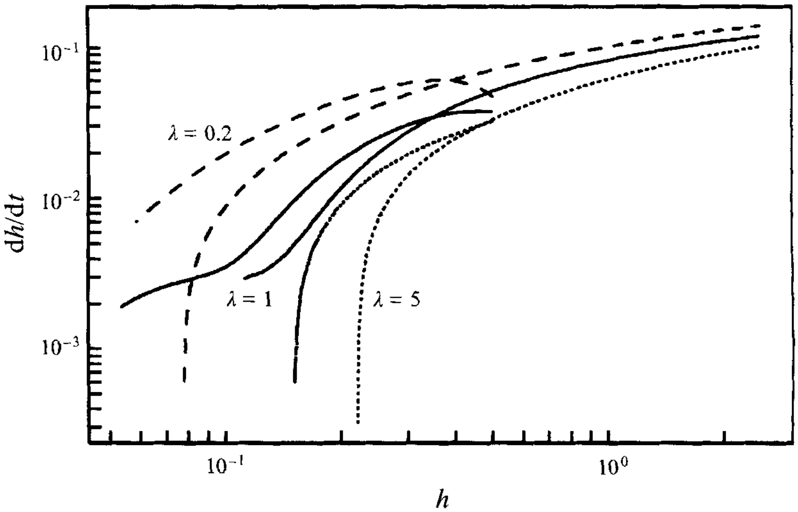

FIGURE 9. The effects of initial drop separation distances. Examples are shown for $\lambda = 0.2$, 1 and 5 with $\mathscr{B} = 10$ and initial separation distances of $0.5a_1$ and $2.5a_1$; $a_1/a_2 = 2$. The initial configuration does not change results qualitatively.

characteristic of small Bond numbers, $\mathscr{B} \ll 1$, and not surprisingly differs significantly from the behaviour of moderately distorted drop pairs characteristic of larger Bond numbers, $\mathscr{B} > 1$. Exact solutions in bipolar coordinates for spherical drops (Haber, Hestroni & Solan 1973) are reasonably accurate for deformable drops when separation distances are large and thus the drops have not distorted to a significant degree. As the separation distance decreases, the analytical result for the rate of approach overpredicts the deformable drop result. The calculated and analytical results differ by less than 10% for separation distances greater than $0.8a_1$ for $\mathscr{B} = 10$ and $0.07a_1$ for $\mathscr{B} = 1$.

Although the drops for $\mathscr{B} = 1$ appear to be nearly spherical (figure 6, drop c), the inset of figure 10 shows a magnification of the thin gap between the deformable drops (solid line) and undeformed spherical drops with the same volume (dashed line). Clearly, the area over which fluid in the gap is squeezed is larger for the deformed drops, and the mode of film flow is characterized by uniform drainage. For comparison, the results of Yiantsios & Davis (1990) show that for drops with $\mathscr{B} \ll 1$ approaching a deformable surface, the rate of film drainage decreases from $\mathrm{d}h/\mathrm{d}t \propto h^{\frac{1}{2}}$ for large and moderate gap thicknesses h, characteristic of spherical drop solutions (Davis *et al.* 1989; Haber *et al.* 1973) to $\mathrm{d}h/\mathrm{d}t \propto h^4$ along the axis of symmetry and $\mathrm{d}h/\mathrm{d}t \propto h^{5/2}$ for the minimum gap thickness (at the rim of the dimple) when h becomes very small. For comparison, we find numerically that $\mathrm{d}h/\mathrm{d}t \propto h^{4.3}$ at $h = 0.02$ and $r = 0$ for the simulation with $\mathscr{B} = 1$ in figure 10.

3.6. *Cusps and tails*

In the experiments (later stages in figure 1) and in the calculations (e.g. figure 6, drop h), regions of very high curvature develop at the back of the trailing bubble or drop. Two features of the flow contribute to the development and maintenance of interface shapes with high curvatures. First, by analogy to the formation of pointed ends on a drop in a steady extensional flow, where the radius of curvature of the end of the drop scales as $\mathscr{B}^{-3}$ (e.g. Acrivos 1983), we might expect that the flow behind the trailing

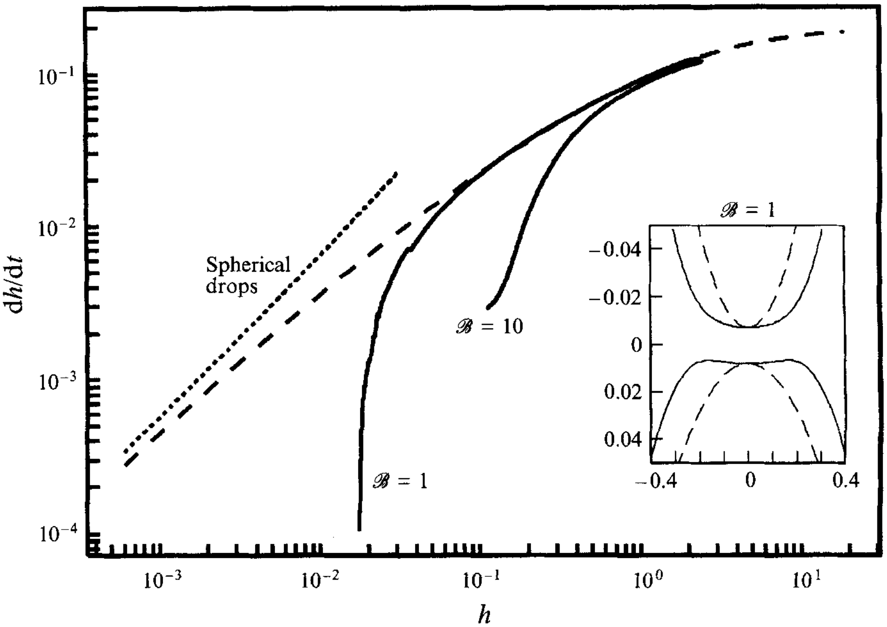

FIGURE 10. Comparison of boundary integral results with analytical results for spherical drops; $\lambda = 1$; $a_1/a_2 = 2$. Numerical results are shown by solid curves for $\mathscr{B} = 1$ and $\mathscr{B} = 10$. The bipolar coordinate solution is shown by a dashed curve (Haber *et al.* 1973). The combined lubrication theory and boundary integral analysis for spherical drops is shown by a dotted line (Davis *et al.* 1989). The inset shows a (distorted) magnification of the geometry of the gap between the drops with solid curves for $\mathscr{B} = 1$ at $h = 0.02$; the shapes of spherical drops with the same volume are shown by dashed curves.

drop, which locally resembles an extensional flow, may allow a tail with a region of high curvature to develop. Second, while the spherical drop shape exactly satisfies the normal stress balance (Batchelor 1967) and is stable to infinitesimal distortions for $\mathscr{B} < \infty$, the effect of the leading drop is to allow the trailing drop to become prolate, and thus to become unstable for large Bond numbers (Koh & Leal 1989; Pozrikidis 1990). The combination of the local extensional flow and a distorted prolate shape allow the drop to be extended and the tail to develop.

Regions of very high curvature also develop at the rim or edge of the coating drop (see figure 1 and figure 6, drop h) where the flow is locally extensional. Near the rim of the coating drop the flow is locally two-dimensional since the thickness of the coating drop is much smaller than the radius of the larger drop.

Recent studies of two-dimensional free-surface flows by Joseph *et al.* (1991) and Jeong & Moffatt (1992) have demonstrated that regions of very high curvature, which may appear macroscopically to be cusps, may develop even for systems with finite interfacial tension. The two-drop interactions shown here fall into the category of flows which allow regions of high curvature to develop.

4. Interaction and stability of offset drops

In this section we consider the stability of the axisymmetric drop configuration studied in § 3. Stability is examined by considering the tendency for an initially off-axis configuration to evolve either towards or away from an aligned configuration. Again we will consider the case of a large drop translating behind a smaller drop; however, the centres-of-mass are initially offset horizontally. Experimental results are presented in §4.1, and a qualitative explanation for the evolution of off-axis configurations is presented in §4.2. Numerical solutions of an analogous two-dimensional geometry are presented in §4.3 to provide an improved quantitative understanding.

In general the two-drop free-boundary problem is difficult for non-aligned drops, and numerical solutions are complicated by the necessity of treating three-dimensional geometries. Previous analytical studies of two-drop interactions have been limited to spheres. Some of the features characteristic of drop interaction and deformation at low Reynolds numbers have been observed in finite-difference/front-tracking numerical studies at finite Reynolds numbers for both two-dimensional and three-dimensional drops (Unverdi & Trygvasson 1992).

The interactions between two drops model a great many two-body interactions common in multiphase sedimentation processes. The results presented below demonstrate that sufficiently deformable drops (moderate Bond numbers, low viscosity ratios) with only modest horizontal displacements will interact in a manner which induces alignment. The alignment of deformable drops owing to hydrodynamic interactions increases the likelihood of coalescence of buoyancy-driven drops. Hence final configurations similar to the results presented in §3 are obtained. We note that drop interaction and alignment may produce uneven concentrations of drops and bubbles in dispersed multiphase systems, analogous to the inhomogeneities which develop in suspensions of non-spherical particles (e.g. Koch & Shaqfeh 1989).

4.1. *Experimental results*

In figures 11 and 12 we show examples of two types of interactions between air bubbles rising in a large container of corn syrup. The interactions leading to alignment arise as a consequence of the *deformation* of the bubbles. The Reynolds numbers in these experiments are small, $\mathscr{R} \approx 5 \times 10^{-3}$, and the Bond numbers are large, $\mathscr{B} \approx 50$.

The experiment in figure 11 illustrates a process we will refer to as drop alignment. In this case the long-range, interaction-induced deformation of the bubbles leads to a lateral component of translation and the eventual alignment of the bubbles. The two bubbles start about one bubble radius apart and eventually align and coalesce over a translational distance of about five drop radii.

The experiment in figure 12 illustrates a short-range process in which the small bubble is advected around the larger bubble and is 'sucked' or entrained into the larger bubble, finally translating vertically with an almost axisymmetric configuration prior to eventually coalescing. The bubbles in figure 12, as well as those in figures 1 and 11, coalesce within 5–30 s after the last photograph shown. The difference between the experiments shown in figures 11 and 12 is that in figure 12 the initial horizontal separation distance was large enough that the small bubble does not coat the larger trailing bubble.

The experimental results indicate that the axisymmetric two-drop configuration studied in §3 is a stable geometry in the limit of large Bond numbers since bubble and drop deformations lead to alignment. For both experiments shown in figures 11 and 12 we note the large degree and complexity of deformation of both bubbles and the formation of tails or regions of high curvature.

4.2. *Flow-induced deformation leading to alignment*

As a preliminary, we note that the corresponding problem of two translating spherical drops evolves so that, relative to a reference frame translating with the larger sphere,

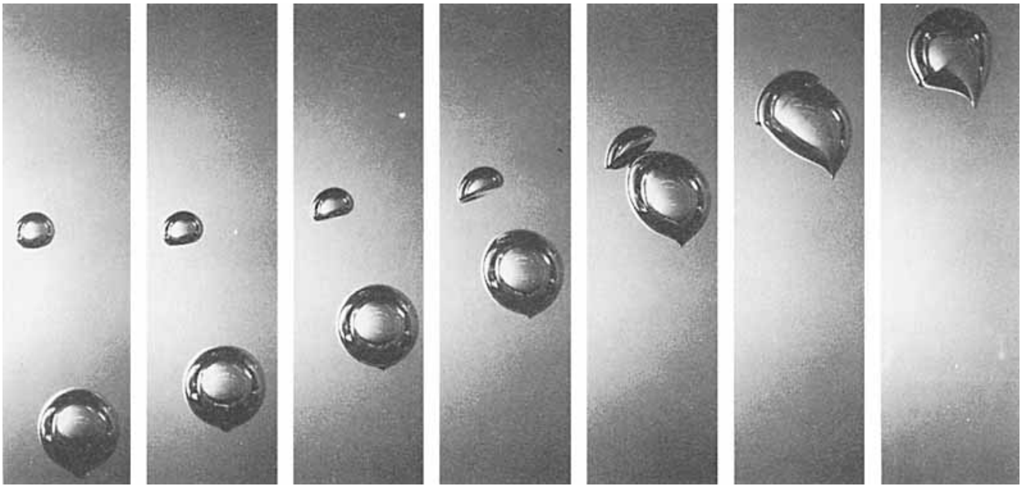

FIGURE 11. Sequence of photographs showing the interaction of initially offset air bubbles in corn syrup, with $\mathscr{B} \approx 50$ and $\mathscr{R} \approx 5 \times 10^{-3}$. Photographs are shown at 5 s intervals. The bubbles coalesce about 10 s after the last photograph shown.

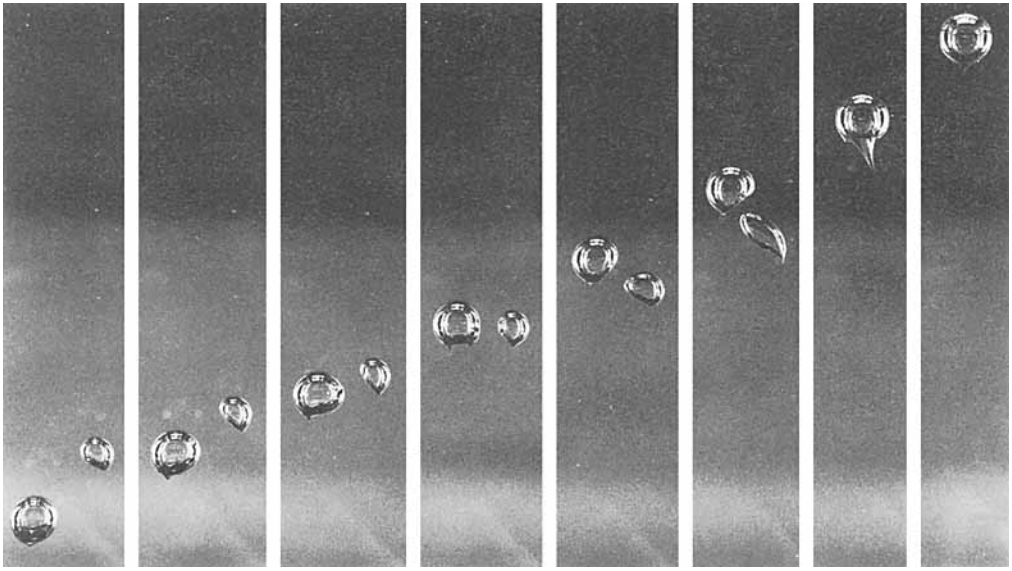

FIGURE 12. Sequence of photographs showing the interaction of initially offset air bubbles in corn syrup, with $\mathscr{B} \approx 50$ and $\mathscr{R} \approx 5 \times 10^{-3}$. Photographs are shown at 10 s intervals. The bubbles coalesce within about 30 s after the last photograph shown.

the small sphere is swept around toward the back, as shown in figure 13. The off-axis configuration is clearly unstable as a consequence of the hyperbolic stagnation point at the front of the larger drop.

For the dynamics shown in figure 11, it is straightforward to provide a qualitative explanation, schematically illustrated in figure 14, for the alignment of offset deformable drops. The alignment occurs since the long-range effect of drop interactions (figure 4) is to deform the trailing drop into a prolate shape, suitably inclined with

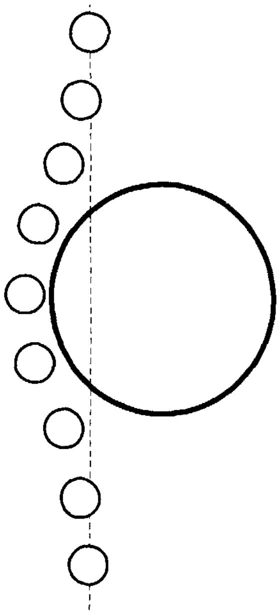

FIGURE 13. Illustration of the interaction between non-deformable spherical drops. Owing to the reversibility property of Stokes flows, the horizontal offset between the drops is preserved as the small drop is swept around the larger drop.

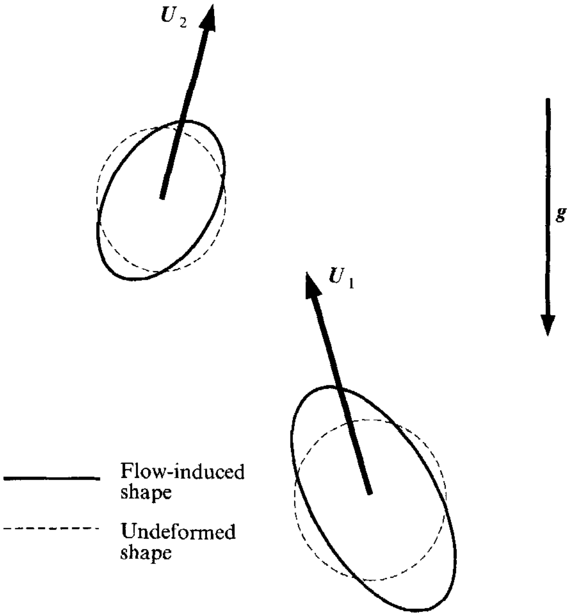

FIGURE 14. Illustration of the mechanism for the alignment of two rising deformable drops. The deformation of each drop by the flow produced by the other drop, as shown in figure 4, allows the drops to translate with velocities U_1 and U_2 which have horizontal components that favour alignment.

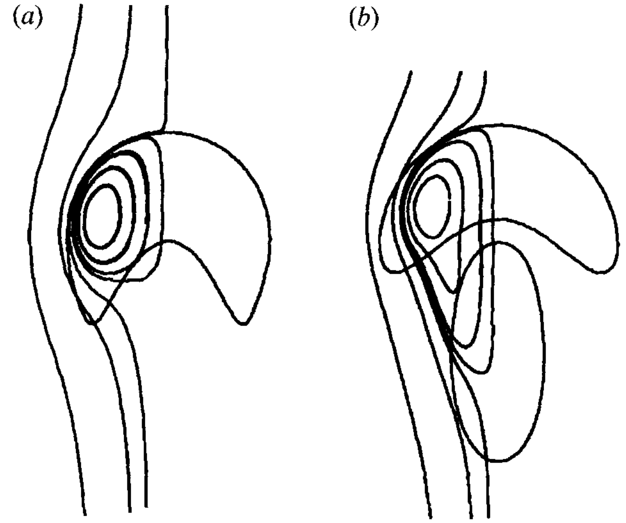

FIGURE 15. Streamlines, relative to the translating drop, (*a*) for a single deforming drop, and (*b*) for a pair of drops (the volume of the trailing drop is $\frac{1}{4}$ the volume of the leading drop); $\mathscr{B} = 50$; $\lambda = 1$. Notice that the streamlines leave the drop and travel through the developing cavity at the back of the drop. Thus, fluid elements in this cavity will be entrained into the drop. The effect of the second drop is to further extend the vortex outside the leading drop. An axisymmetric geometry is assumed and the streamlines are calculated using the boundary integral method described in § 2.

respect to the vertical; the leading drop is deformed into an oblate shape. Owing to the deformation, each drop has a horizontal component of velocity in a direction opposite to that shown in figure 13. If deformation is sufficiently large, the horizontal velocities may favour alignment, as indicated in figure 14. In § 5 we calculate the deformation-induced velocity.

We suggest that the second type of two-drop interaction (figure 12), in which the small drop is first advected around the larger drop and then sucked in from behind, is the result of short-range dynamics owing to the deformation of the larger drop. The dynamics are dictated by the continual deformation of the larger drop so that in a frame of reference moving with the larger drop, streamlines will not be contained entirely within the drop, as they are for spherical drops. Deformation at the back of the drop results in closed streamlines which leave and re-enter the drop, defining a vortex shown in figure 15(*a*) for an axisymmetric drop. Thus, a neutrally buoyant fluid element in the region behind the leading drop may be advected into the cavity which develops behind the deforming leading drop. In figure 15(*b*) we show streamlines (again in a frame of reference moving with the front of the leading drop) for an axisymmetric two-drop geometry (the volume of trailing drop is $\frac{1}{4}$ the volume of the leading drop). The effect of the second drop is to increase the extent of the vortex outside the leading drop. A sufficiently deformable drop partly located in the vortical region will tend to be entrained. At higher Reynolds numbers a similar phenomenon occurs for two spherical drops owing to the formation of a low-pressure wake. We emphasize the distinction between the high Reynolds number dynamics, and the low Reynolds number dynamics shown in figure 12 which rely on the deformation of the drop.

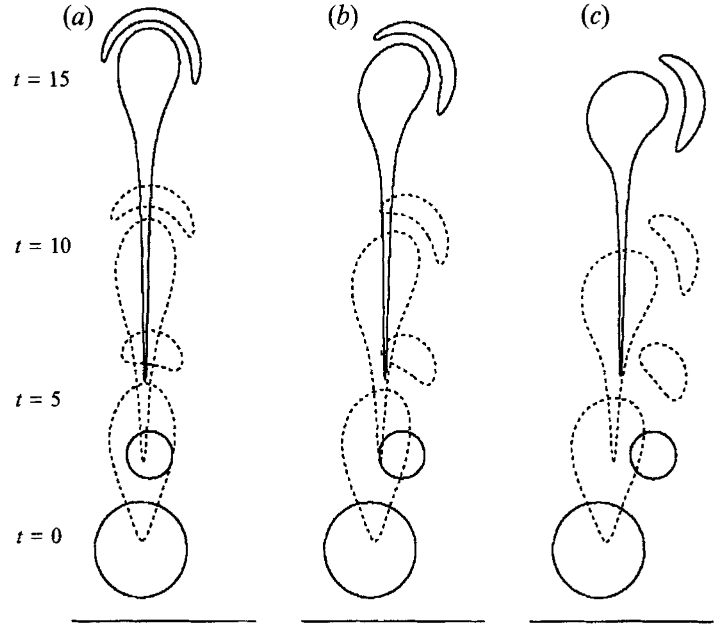

FIGURE 16. The effect of initial configuration. Results are shown for three different offsets; $\lambda = 1$; $\mathscr{B} = \infty$; $a_1/a_2 = 2$. The horizontal line represents a free-slip lower planar surface.

4.3. *Numerical results*

A full three-dimensional treatment of the boundary integral equations (the geometry required to study offset drops) requires the numerical description of a twice-differentiable three-dimensional surface. The boundary integral method has been used to study three-dimensional free-surface problems, but has been limited to modest deformations (e.g. de Bruijn 1989; Pozrikidis 1992*b*). We introduce a simplification and consider two-dimensional (cylindrical) drops. This geometry allows us to consider the most important feature of the problem, namely, the horizontal offset. To the extent that such two-dimensional simulations represent the important dynamical processes of the three-dimensional problem, the results presented below provide an improved understanding of the nature of two-drop interactions. We will see that the two-dimensional calculations reproduce the qualitative behaviour of two-drop systems for both types of interactions observed in the experiments shown in figures 11 and 12.

The boundary integral method has had limited application to two-dimensional free-boundary problems (e.g. Newhouse & Pozrikidis 1990). An important consideration with two-dimensional Stokes flows is the logarithmic behaviour of the velocity kernel which in unbounded domains leads to Stokes paradox. We eliminate this difficulty by including a planar free-slip lower surface; boundary conditions for the planar surface are accounted for by using the appropriate image system. This boundary has the physical effect of creating tails on drops due to viscous resistance by the planar surface. However, the development of a tail does not have a noticeable effect on the dynamics of drop interaction. The parameters which describe the two-dimensional problem are the same as the parameters describing axisymmetric drops. The numerical implementation follows the discussion given in § 2; the kernel functions and image singularities are given in Appendix B.

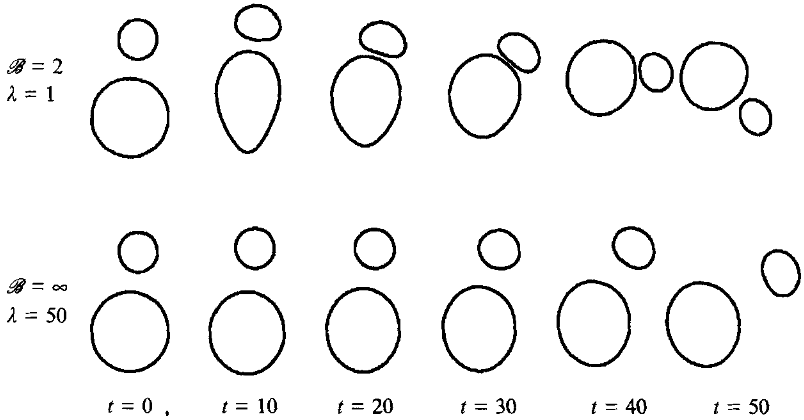

FIGURE 17. The effect of interfacial tension and drop viscosity on drop interactions illustrated in a frame of reference translating with the drops. The initial geometry is the same as the initial geometry in figure 16(*a*). Calculations are shown for $\lambda = 1$, $\mathscr{B} = 2$ and $\lambda = 50$, $\mathscr{B} = \infty$; $a_1/a_2 = 2$. For both cases the small drop is swept around the leading drop, whereas in figure 16(*a*) the small drop coats the large drop. The horizontal planar surface is not shown.

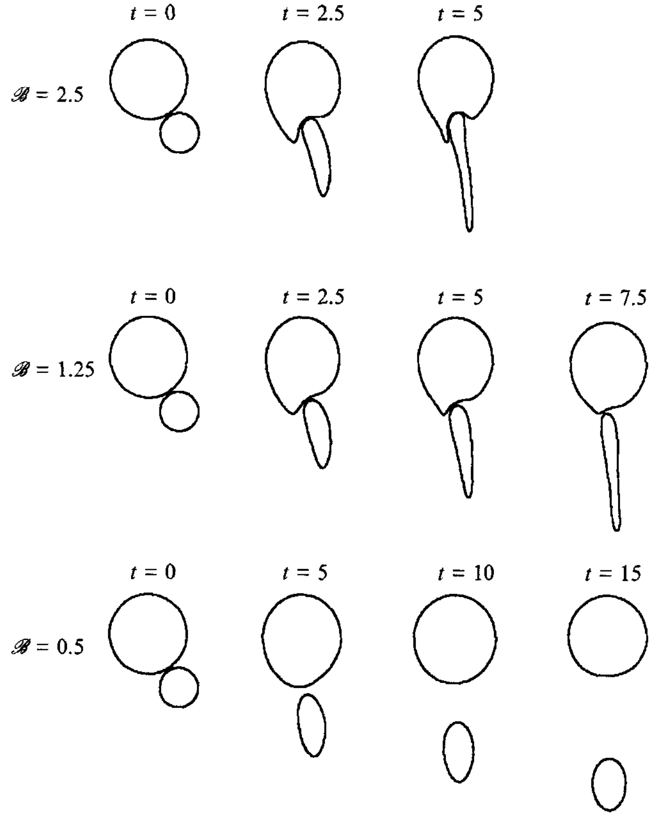

FIGURE 18. The effect of interfacial tension on the interactions between a small drop trailing a larger drop illustrated in a frame of reference moving with the drops. Calculations are shown for $\mathscr{B} = 2.5, 1.25$ and 0.5; $\lambda = 0.1$; $a_1/a_2 = 1/2$ (Bond number based on the trailing drop). For large enough Bond numbers, the small drop may be sucked into the larger drop owing to the deformation of the larger drop. The horizontal planar surface is not shown.

In figure 16 we show three simulations for different horizontal offsets for the case $\lambda = 1$ and zero interfacial tension. As the initial horizontal offset increases, the tendency of the smaller leading drop to spread over the larger trailing drop decreases. Even for large offsets, the deformation of the leading drop is large owing to the long-range nature of Stokes flows. For the axisymmetric two-drop interactions studied in § 3, a tail develops on the trailing drop owing to the deformation induced by the leading drop and the natural instability of non-spherical shapes when the interfacial tension is small (Kojima *et al.* 1984); the tail which develops in the two-dimensional calculations is larger because of the presence of a nearby free-slip surface.

In figure 17 we show that provided the drops can sufficiently resist deformation, by either having a large viscosity contrast or large interfacial tension, then the small drop may be swept around the large drop. Specifically we show calculations for $\lambda = 50$ and $\mathscr{B} = \infty$, and $\lambda = 1$ and $\mathscr{B} = 2$. Since the drops translate very large distances in the simulations shown in figure 17, typically about 40 drop radii, we show drop shapes at different times in a frame of reference moving with the drops. The initial drop configuration is the same as the initial configuration for the drops shown in figure 16(*a*). In both cases shown in figure 17 the small drop is swept around the large drop. However, the interaction between the two drops differs in the two cases. For large viscosity ratios (such as the $\lambda = 50$ case) the separation distance between the drops remains large since the fluid between the drops is squeezed out slowly owing to the small amount of flow in the drop. For the case of $\lambda = 1$ the fluid can drain more quickly and the separation distance may become small (e.g. $\mathscr{B} = 2$, $t = 30$).

Finally, in figure 18, we illustrate the importance of drop deformation on the 'suction' or entrainment of a small trailing drop by a larger drop. As in figure 17, we show drop shapes at different times in a frame of reference translating with the front of the large drop. Simulations are shown for $\lambda = 0.1$ (which allows for rapid and larger drop distortions) and $\mathscr{B} = 0.5$, 1.25 and 2.5 (where the Bond number is based on the radius of the smaller trailing drop). For large interfacial tension, $\mathscr{B} = 0.5$, the small drop is left behind. Notice however that the drops are eventually aligned. For smaller interfacial tension, $\mathscr{B} = 2.5$, the larger drop is indented and the trailing small drop is advected into the developing cavity. At times greater than $t = 5$ the drops numerically make contact and the simulation is stopped. In the two-dimensional simulations, we found that the initial separation distance needed to be very small in order for the small drop to be entrained into the larger drop. This quantitative feature is not characteristic of the experimental results presented in figure 12.

5. Long-range drop interactions

In this section we study analytically the lateral translation of two drops arising from their interaction-induced deformation. We demonstrate explicitly that the amount of deformation, controlled primarily by the Bond number and the separation distance between two drops, determines whether two drops will eventually coalesce.

There are three analytical features necessary to calculate the shape-induced migration. The method of reflections (e.g. Happel & Brenner 1965; Leal 1992) is used in § 5.2 to determine the approximate velocity field in the neighbourhood of each drop. The local velocity gradient deforms the drop and the deformation is calculated in § 5.3 using standard procedures for nearly spherical, distorted drops. The translational velocity induced by the non-spherical shape is then calculated in § 5.4 using the Reciprocal theorem (e.g. Haj-Hariri, Nadim & Borhan 1990). We will assume for simplicity that both drops are composed of the same fluid.

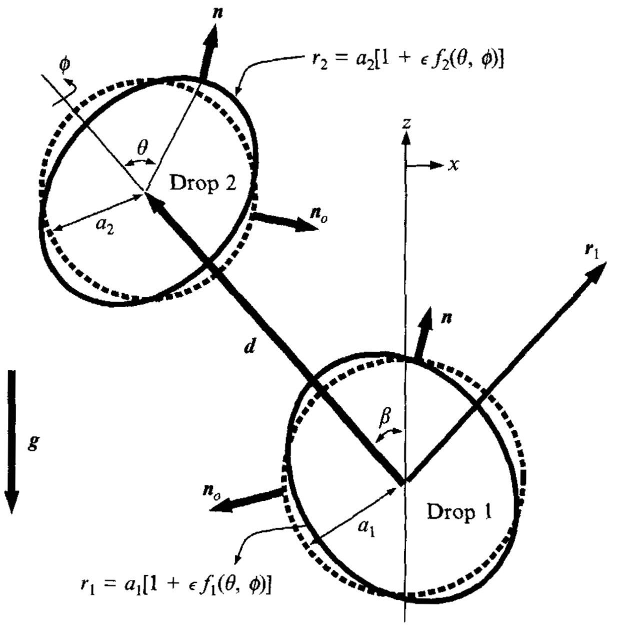

FIGURE 19. Geometry of the two-drop problem and definition of the normals $\boldsymbol{n}$ and $\boldsymbol{n}_o$. Drops 1 and 2 have radii a_1 and a_2, respectively, are separated by a distance d, and are oriented at angle β with respect to gravity.

5.1. *Scaling analysis: an overview of drop alignment by flow-induced shape changes*

Consider two widely separated drops, labelled 1 and 2, rising in an unbounded fluid at low Reynolds numbers (figure 19). The vector $\boldsymbol{d}$ indicates the direction and magnitude of the separation between the centres of the two drops. We will always choose drop 1 to be the trailing drop.

Each drop will rise, to a first approximation, as though alone in an unbounded fluid. The rise speed as a function of the viscosity ratio λ is given by the Hadamard–Rybczyński result

$$\boldsymbol{U}_i^{(0)} = -\frac{2(1+\lambda)}{3(2+3\lambda)}\frac{\Delta\rho a_i^2}{\mu}\boldsymbol{g}, \quad i = 1, 2, \tag{5.1}$$

where the subscript i is used to denote drops 1 or 2.

Drop 2 experiences an $O(U_1^{(0)}a_1/d)$ change in the Hadamard–Rybczyński velocity owing to the long-range interaction with drop 1. If the drops remain spherical, the next correction to the rise speed is $O(U_1^{(0)}a_1^3/d^3)$ (Kim & Karrila 1991). However, when deformation occurs, we will show that there is a translational velocity component due to the non-spherical shape. Let ϵ measure the small distortion away from a spherical shape. The far-field velocity gradient generated by drop 1 in the vicinity of drop 2 is U_1a_1/d^2. A balance of viscous stresses, $\mu U_1 a_1/d^2$, by the interfacial tension stresses of drop 2, $\epsilon\sigma/a_2$, which tend to keep the drop nearly spherical, leads to a small shape distortion with magnitude

$$\epsilon = \frac{g a_1^3 a_2 \Delta\rho}{\sigma d^2} = \mathscr{B}\left(\frac{a_1 a_2}{d^2}\right). \tag{5.2}$$

A similar analysis for drop 1 gives $\epsilon = \mathscr{B}a_2^3/a_1 d^2$.

We note that the small drop is always more deformed than the larger drop (see figures 1, 3, 11 and 12). Although restoring interfacial tension stresses are larger for small drops, scaling as $\epsilon\sigma/a_2$ for drop 2, the viscous stresses deforming drop 2 are proportional to a_1^3. Thus, the size of the other drop controls the magnitude of drop distortion. By contrast, for $\mathscr{B} \ll 1$, the larger drop becomes more deformed than the smaller drop (Yiantsios & Davis 1991).

The small distortions are oblate for the leading drop and prolate for the trailing drop, e.g. figure 4. We will demonstrate that the $O(\epsilon)$ shape distortion leads to an $O(\epsilon U_1^{(0)})$ contribution to the drops' translational velocity, with particular importance assigned to the horizontal component of translation which may lead to alignment. Thus, drop alignment depends on the relative magnitudes of a/d and ϵ. We will show that drop deformation should lead to drop alignment when

$$\mathscr{B} > O\left(\frac{d}{a}\right). \tag{5.3}$$

Nevertheless, there is an upper bound on the small-deformation analysis we describe which requires $\mathscr{B} < O(d/a)^2$.

A quasi-steady small distortion is assumed implicitly to derive equation (5.2); the drop deforms, in response to the viscous stresses created by the motion of the second drop, on a timescale τ_d that is less than the timescale τ_a over which the separation distance d changes. Estimates of these timescales for drop 2 are

$$\tau_d \approx a_2(1+\lambda)\mu/\sigma \quad \text{and} \quad \tau_a \approx d/|U_1 - U_2|, \tag{5.4}$$

where the factor of $1+\lambda$ indicates that the largest fluid viscosity controls the rate of drop deformation. The quasi-steady assumption neglects explicit time-dependence in the free-boundary problem, and thus requires that

$$\mathscr{B} < \frac{d}{(1+\lambda)|1 - a_2^2/a_1^2|a_2}. \tag{5.5}$$

For nearly equal-sized drops, large separation distances, and $\lambda < O(1)$ the right-hand side of equation (5.5) is very large and the assumption of rapid shape adjustment to changes in the local flow is justified. For (5.3) and (5.5) to be consistent the drops must have similar radii so that the local flow near either drop changes slowly. For equal-sized drops, $\tau_a \approx \epsilon U^{(0)}$ (see § 5.4), and thus leads to the constraint $\mathscr{B}^2 < O(d^3/a^3)$ which is less restrictive than (5.5). The quasi-steady assumption, though restrictive, is assumed in the analysis below.

5.2. *Migration of spherical drops: application of the method of reflections*

As a first approximation we assume the drops are spherical. Let $\boldsymbol{r}_i$ denote the position vector relative to the centre of drop i (see figure 19). The velocity field due to the translation of drop i in an unbounded fluid is

$$\boldsymbol{u}_i^{(0)}(\boldsymbol{r}_i) = \frac{2\pi(2+3\lambda)}{1+\lambda} a_i \left[1 + \frac{\lambda a_i^2}{2(2+3\lambda)} \nabla^2\right] \boldsymbol{J}_i \cdot \boldsymbol{U}_i^{(0)}, \tag{5.6}$$

where

$$\boldsymbol{J}_i(\boldsymbol{r}_i) = \frac{1}{8\pi}\left(\frac{\boldsymbol{I}}{r_i} + \frac{\boldsymbol{r}_i\boldsymbol{r}_i}{r_i^3}\right). \tag{5.7}$$

$\boldsymbol{U}_i^{(0)}$ is the Hadamard–Rybzcyński velocity given by equation (5.1), and the superscript (0) is used to denote the first approximation to the detailed velocity field.

Each drop will move faster owing to the interaction with the far-field flow produced by the other drop. The change in translational velocity is proportional to the speed of the other drop, so has magnitude $O(U^{(0)}a/d)$. The corrected rise speed of drop 1 is caused by drop 2 and has a value $\boldsymbol{u}_2^{(0)}(\boldsymbol{r}_2 = \boldsymbol{d})$; thus drop 1 translates with velocity

$$\begin{aligned} \boldsymbol{U}_1 &= \boldsymbol{U}_1^{(0)} + \left(\frac{a_2}{d}\right) \boldsymbol{U}_1^{(1)} + O(U_2^{(0)} a_2^3/d^3) \\ &= \boldsymbol{U}_1^{(0)} + \frac{(2+3\lambda)}{4(1+\lambda)} \frac{a_2}{d} \left[\boldsymbol{U}_2^{(0)} + \boldsymbol{U}_2^{(0)} \cdot \hat{\boldsymbol{d}}\hat{\boldsymbol{d}}\right] + O\left(U_2^{(0)} \frac{a_2^3}{d^3}\right), \end{aligned} \tag{5.8}$$

where $\hat{\boldsymbol{d}} = \boldsymbol{d}/|\boldsymbol{d}|$ is a unit vector in the direction of the line-of-centres of the two drops, directed from drop 1 to drop 2 (figure 19). Similarly, drop 2 rises with velocity

$$\boldsymbol{U}_2 = \boldsymbol{U}_2^{(0)} + \frac{(2+3\lambda)}{4(1+\lambda)} \frac{a_1}{d} \left[\boldsymbol{U}_1^{(0)} + \boldsymbol{U}_1^{(0)} \cdot \hat{\boldsymbol{d}}\hat{\boldsymbol{d}}\right] + O\left(U_1^{(0)} \frac{a_1^3}{d^3}\right). \tag{5.9}$$

The horizontal separation distance between the drops increases or decreases due to the difference in horizontal velocities, $\Delta U_H = (\boldsymbol{U}_1 - \boldsymbol{U}_2) \cdot \boldsymbol{e}_x$, given by

$$\Delta U_H = \frac{\Delta\rho g a_1^3}{6\mu d} \sin\beta \cos\beta \left[1 - \left(\frac{a_2}{a_1}\right)^3\right], \tag{5.10}$$

where we observe that equation (5.10) is independent of the viscosity ratio λ. We note that if drop 1 is larger than drop 2, the case of interest here, then the horizontal separation distance will increase for spherical drops ($\Delta U_H > 0$), whereas if drop 2 is larger than drop 1 the separation distance will decrease ($\Delta U_H < 0$), in agreement with the illustration shown in figure 13. In the following section we consider the correction to the translational velocity arising from drop deformation with magnitude $\mathscr{B}(a/d)^2$, e.g. equation (5.2). For the horizontal separation distance to decrease (for the drops to align as in figures 11 and 14) we then require that $\mathscr{B} > O(d/a)$ to counteract the drifting described by equation (5.10).

5.3. *Shape calculation*

The contribution of the second reflection to the flow field due to translating spherical drops produces corrections that are $O(U^{(0)}a^3/d^3)$ (Kim & Karrila 1991). The corrections due to the second reflection are smaller than the high Bond number non-spherical shape corrections which we now describe.

In the vicinity of drop 2 the velocity field produced by drop 1 may be represented as a Taylor series

$$\boldsymbol{u}_1(\boldsymbol{r}_1 = \boldsymbol{d} + \boldsymbol{r}_2) = \boldsymbol{u}_1|_{\boldsymbol{r}_1=\boldsymbol{d}} + \boldsymbol{r}_2 \cdot \nabla \boldsymbol{u}_1|_{\boldsymbol{r}_1=\boldsymbol{d}} + \dots. \tag{5.11}$$

The velocity gradient $\nabla \boldsymbol{u}_1|_{\boldsymbol{r}_1=\boldsymbol{d}}$ in the neighbourhood of drop 2 is responsible for drop deformation. Using the velocity field in equation (5.6) we find that

$$\nabla \boldsymbol{u}_1|_{\boldsymbol{r}_1=\boldsymbol{d}} = -\frac{(2+3\lambda)a_1}{4(1+\lambda)d^2} \left[\boldsymbol{I}\hat{\boldsymbol{d}} \cdot \boldsymbol{U}_1^{(0)} - 3\hat{\boldsymbol{d}}\hat{\boldsymbol{d}}\hat{\boldsymbol{d}} \cdot \boldsymbol{U}_1^{(0)} - \hat{\boldsymbol{d}}\boldsymbol{U}_1^{(0)} + \boldsymbol{U}_1^{(0)}\hat{\boldsymbol{d}}\right]. \tag{5.12}$$

We will assume that the deformed shape of drop 2 may be described in spherical coordinates (r, θ, ϕ) by

$$r_2 = a_2\left[1 + \epsilon f_2(\theta, \phi)\right], \tag{5.13}$$

where $\epsilon \ll 1$. A drop immersed in a linear flow, $\boldsymbol{r}_2 \cdot (\nabla \boldsymbol{u}_1)$, is distorted into an ellipsoidal shape (Taylor 1932), described by

$$\epsilon f_2(\theta, \phi) = \frac{\mu a_2(16+19\lambda)}{8\sigma(1+\lambda)} \boldsymbol{n}_o \cdot (\nabla \boldsymbol{u}_1) \cdot \boldsymbol{n}_o, \tag{5.14}$$

where $\boldsymbol{n}_o$ is a unit normal to a spherical drop. In the derivation of (5.14) the quasi-steady boundary condition $\boldsymbol{u} \cdot \boldsymbol{n}_o = 0$ is used. This approximation is justified provided the timescale for drop deformation by viscous stresses is shorter than the timescale for changes in the local flow producing the deformation, as discussed in § 5.1. Thus, using equations (5.12)–(5.14) and the definition of the Bond number given by equation (2.7), the steady deformed shape of each drop is an ellipsoid described by second-degree Legendre polynomials as

$$r_2 = a_2 \left[1 + \mathscr{B}\left(\frac{a_2}{a_1}\right)\left(\frac{a_1}{d}\right)^2 \frac{16+19\lambda}{48(1+\lambda)}\left[1 - 3(\hat{\boldsymbol{d}} \cdot \boldsymbol{n}_o)^2\right]\cos\beta\right] \tag{5.15}$$

and

$$r_1 = a_1 \left[1 - \mathscr{B}\left(\frac{a_2}{a_1}\right)\left(\frac{a_2}{d}\right)^2 \frac{16+19\lambda}{48(1+\lambda)}\left[1 - 3(\hat{\boldsymbol{d}} \cdot \boldsymbol{n}_o)^2\right]\cos\beta\right], \tag{5.16}$$

where the orientation angle β is defined in figure 19. The drop shapes in the experiments in figures 1, 11 and 12 and the numerical calculations eventually lose the ellipsoidal symmetry as the separation distance a/d becomes order one and ϵ becomes large.

In equations (5.15) and (5.16) the small parameter ϵ can be identified as $\mathscr{B}a_1a_2/d^2$ for drop 2 (as deduced in § 5.1) and $\mathscr{B}a_2^3/a_1d^2$ for drop 1. For simplicity, in the discussion that follows we refer to the small deformation of either drop as having magnitude $O(\mathscr{B}a^2/d^2)$.

As expected on physical grounds, or from a sketch of the streamlines, the leading drop deforms into an oblate spheroidal shape whereas the trailing drop is deformed into a prolate spheroidal shape. We may expect by analogy to the motion of ellipsoidal rigid particles in low Reynolds number flows that the ellipsoidal shapes will migrate in a manner tending to promote on-axis configurations (and possibly coalescence). We now calculate explicitly this translational velocity. Rather than solving for the flow field and then computing the translational velocity, we will use the Reciprocal theorem to provide a direct calculation of the velocity.

5.4. *Translational velocity from the Reciprocal theorem*

The above analysis suggests a small $O(\mathscr{B}a^2/d^2)$ correction to the local description of the flow field owing to the drop's deformation. Since a/d and $\mathscr{B}$ are independent parameters we seek the next-order correction to the velocity field, $\mathscr{B}(a/d)^2\boldsymbol{u}^{(2)}(\boldsymbol{r})$, satisfying the Stokes equations both inside and outside the drop. This analysis corresponds to the translation of an isolated slightly deformed drop in an otherwise quiescent fluid. Thus, we seek solutions for the approximate translational velocity in the form

$$U(a/d, \mathscr{B}) = U^{(0)} + \left(\frac{a}{d}\right)U^{(1)} + \mathscr{B}\left(\frac{a}{d}\right)^2 U^{(2)} + O\left(U^{(0)}\frac{a^3}{d^3}\right). \tag{5.17}$$

Provided $\mathscr{B} > O(d/a)$ the dominant correction to the migration velocity arises from the third term on the right-hand side. Furthermore, so long as $\mathscr{B} > O(a/d)$, shape modifications are at least as important as the $O(a/d)^3$ corrections calculated using the method of reflections for spherical drops.

The boundary conditions satisfied by $\boldsymbol{u}^{(2)}(\boldsymbol{r})$ are obtained by using standard domain perturbation techniques whereby all variables are expanded in the neighbourhood of a spherical shape and evaluated at $|\boldsymbol{r}_i| = a_i$. For this part of the analysis it is convenient to non-dimensionalize the equations and boundary conditions. The dimensionless

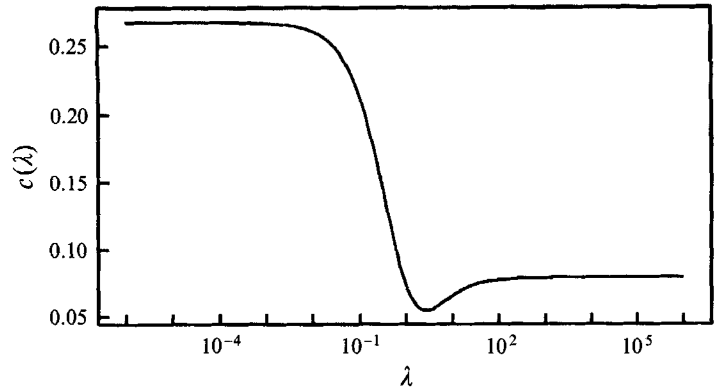

FIGURE 20. The function $c(\lambda)$ defined by equation (5.24).

boundary value problem assumes the form (see Appendix C)

$$\begin{aligned} &\nabla\cdot\boldsymbol{T}^{(2)}=0, \quad r>1, \qquad \nabla\cdot\hat{\boldsymbol{T}}^{(2)}=0, \quad r<1,\\ &\nabla\cdot\boldsymbol{u}^{(2)}=0, \qquad\qquad\ \ \nabla\cdot\hat{\boldsymbol{u}}^{(2)}=0, \end{aligned} \tag{5.18}$$

$$\boldsymbol{u}^{(2)}-\hat{\boldsymbol{u}}^{(2)}=\boldsymbol{A}(\boldsymbol{n}_o,f) \ \text{ on } \ r=1, \tag{5.19}$$

$$\boldsymbol{u}^{(2)}\cdot\boldsymbol{n}_o=B(\boldsymbol{n}_o,f)+\frac{\boldsymbol{U}^{(2)}\cdot\boldsymbol{n}_o}{U^{(0)}} \ \text{ on } \ r=1, \tag{5.20}$$

$$\boldsymbol{n}_o\cdot\boldsymbol{T}^{(2)}-\lambda\boldsymbol{n}_o\cdot\hat{\boldsymbol{T}}^{(2)}=\boldsymbol{C}(\boldsymbol{n}_o,f) \ \text{ on } \ r=1, \tag{5.21}$$

where ^ denotes variables inside the drop. The dimensionless functions A, B and C are derived in Appendix C, and depend on the detailed drop shape $f(\theta,\phi)$.

We can then use the Reciprocal theorem (equation (C35) in Appendix C) to obtain the second-order velocity correction

$$\begin{aligned} \boldsymbol{U}^{(2)}=-\frac{U^{(0)}}{4\pi(2+3\lambda)}\int_S \{&[(1+2\lambda)\boldsymbol{I}+\boldsymbol{n}_o\boldsymbol{n}_o]\cdot\boldsymbol{C}(\boldsymbol{n}_o,f)+3\lambda\,[\boldsymbol{I}-3\boldsymbol{n}_o\boldsymbol{n}_o]\cdot\boldsymbol{A}(\boldsymbol{n}_o,f)\\ &+3(2+3\lambda)B(\boldsymbol{n}_o,f)\boldsymbol{n}_o\}\,\mathrm{d}S, \end{aligned} \tag{5.22}$$

where S denotes a spherical drop surface. Evaluating the integrals we find

$$\boldsymbol{U}_i^{(2)}=(-1)^i c(\lambda)\boldsymbol{U}_i^{(0)}\cdot\hat{\boldsymbol{d}}\left(\boldsymbol{e}_z\cdot\hat{\boldsymbol{d}}\right)\left[\boldsymbol{e}_z-3\boldsymbol{e}_z\cdot\hat{\boldsymbol{d}}\hat{\boldsymbol{d}}\right], \tag{5.23}$$

where $\boldsymbol{e}_z$ is a unit vector in the vertical direction and

$$c(\lambda)=\frac{(16+19\lambda)(8-\lambda+3\lambda^2)}{240(1+\lambda)^2(2+3\lambda)}. \tag{5.24}$$

Note that $c=4/15$ for a bubble, $c=19/240$ for a rigid particle, and c has a minimum value for $\lambda\approx 2.64$. The function $c(\lambda)$ is plotted in figure 20. The condition that the horizontal separation between the drops decreases (see equation (5.17)) is given by $\mathscr{B}(a_2^3/a_1d^2)\boldsymbol{U}_1^{(2)}\cdot\boldsymbol{e}_x-\mathscr{B}(a_1a_2/d^2)\boldsymbol{U}_2^{(2)}\cdot\boldsymbol{e}_x+\Delta U_H<0$, i.e.

$$\mathscr{B}>\frac{d}{a_1}\frac{2+3\lambda}{24(1+\lambda)c(\lambda)\cos^2\beta}\left[\left(\frac{a_1}{a_2}\right)^3-1\right]. \tag{5.25}$$

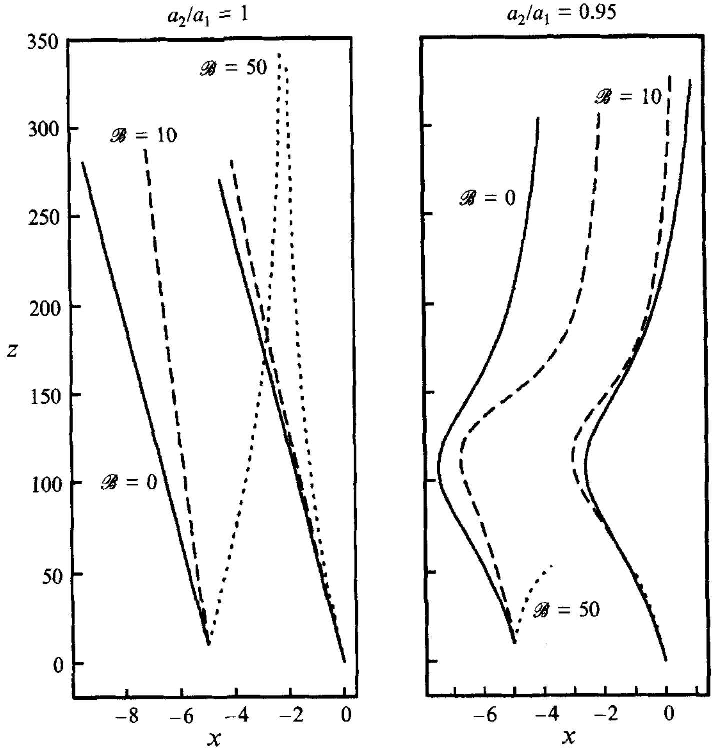

FIGURE 21. Trajectories of two bubbles ($\lambda = 0$) for different values of the Bond number and bubble sizes, in the limit of small deformation. The solid lines are for $\mathscr{B} = 0$, the dashed lines for $\mathscr{B} = 10$, and the dotted lines for $\mathscr{B} = 50$. The curves for $a_2/a_1 = 0.95$ and $\mathscr{B} = 10$ are stopped when the bubbles have aspect ratios greater than 3/2. The bubbles are initially separated by a horizontal distance of $5a_1$ and a vertical distance of $10a_1$.

Using the above results we can integrate the drop velocities to determine the trajectory of a pair of drops, assuming a quasi-steady deformation given by the instantaneous separation distance. In figure 21 bubble trajectories ($\lambda = 0$) are shown for $\mathscr{B} = 0$, 10 and 50, and radii ratios $a_2/a_1 = 1$ and 0.95. The bubbles are separated initially by a horizontal (x) distance of 5 and a vertical (z) distance of 10, where the lengthscale is normalized to the radius of the larger bubble a_1. The vertical lengthscale is compressed significantly. The calculations are stopped when the aspect ratio of one of the bubbles exceeds 3/2.

For the equal-sized bubbles shown on the left, the $\mathscr{B} = 50$ bubbles (trajectories shown with dotted curves) are aligned. For comparison, spherical bubbles ($\mathscr{B} = 0$) drift horizontally maintaining the same orientation and separation distance. Even for the $\mathscr{B} = 10$ simulation there is a noticeable difference in bubble translation compared to the simulation for spherical bubbles. When the leading bubble is smaller than the trailing bubble ($a_2/a_1 = 0.95$), the small bubble is swept around the larger one for small Bond numbers, $\mathscr{B} = 0$ and 10. In the $\mathscr{B} = 50$ simulation, the bubbles are aligned and in real systems would be expected to coalesce eventually. The examples shown in figure 21 demonstrate explicitly the importance of deformation on drop and bubble interactions, particularly for large Bond numbers.

6. Concluding remarks

In this paper we have considered the time-dependent interactions between two low Reynolds number buoyancy-driven deformable drops in the limit that buoyancy forces dominate restoring interfacial tension forces. For axisymmetric configurations, the film drainage between the drops may be characterized by three distinct modes: (i) rapid drainage for which the thinnest region of the film is on the axis of symmetry, (ii) uniform drainage for which the film has a nearly constant thickness, and (iii) dimple formation. As the separation distance between the two drops decreases, the mode of film drainage may change from rapid drainage to uniform drainage and eventually a dimple may form. The numerical calculations presented in § 3 cover Bond numbers $0.25 \leqslant \mathscr{B} < \infty$ and viscosity ratios $0.2 \leqslant \lambda \leqslant 20$. For a given viscosity ratio (e.g. $\lambda = 1$) the separation distances at which the dimple begins to form is larger for intermediate Bond numbers ($\mathscr{B} = 10$) than for very large or very small Bond numbers ($\mathscr{B} = \infty$ and 1). The separation distance between the drops at which a dimple begins to form decreases as the viscosity ratio decreases. Lubrication theory results and combined lubrication theory–boundary integral analyses (Barnocky & Davis 1989; Yiantsios & Davis 1990, 1991; Davis *et al.* 1989), which are appropriate for $\mathscr{B} \ll 1$, differ significantly from the behaviour of drops for $\mathscr{B} > 1$. Exact solutions in bipolar coordinates for spherical drops (Haber *et al.* 1973) are reasonably accurate for deformable drops when drop separation distances are large.

Calculations and experiments with initially offset drops show that the axisymmetric drop configuration is stable for sufficiently deformable drops. A small leading drop may still coat a larger trailing drop, whereas for large enough drop viscosities or small enough Bond numbers, the small drop will be swept around the large drop. In the latter case, if the large drop is sufficiently deformable, the small drop may be sucked or entrained into the large drop as a result of the deformation of the larger drop. In § 5 we showed, using far-field approximations, that deformable drops migrate towards each other provided $\mathscr{B} > O(d/a)$.

Although the spherical-drop assumption allows for the development of many analytical results and approximations, in the limit of moderate to large Bond numbers, typically $\mathscr{B} > 1$, drops become highly deformed, and results based on spherical drops may become invalid. Some characteristics of drop interaction cannot be predicted by assuming spherical drop shapes, such as the alignment of drops owing to interaction-induced deformation and the coating of large drops by smaller drops. Although we have not included the effects of surfactants, we expect that these results may qualitatively describe the behaviour of drops where the interfacial tension is greatly reduced by the presence of surfactants.

Large Bond numbers are characteristic of many problems in solid-earth geophysics and geology because of the large lengthscales in these systems. The Reynolds number is generally much less than 1 since the viscosity of the mantle is about 10^{21} Pa s and the viscosity of magmas ranges from 10 to 10^7 Pa s. For example, mantle plumes, which are believed to be low-viscosity (relative to the rest of the mantle) and low-density instabilities produced in a thermal boundary layer at the base of a convecting mantle, may be described to a good approximation as buoyant drops since the Péclet number is very large (Olson & Singer 1985; Griffiths, Gurnis & Eitelberg 1989). Mantle plumes are thought to consist of a large nearly spherical plume head followed by a tail or conduit attached to the thermal boundary layer (Griffiths & Campbell 1990). On the basis of the results presented in this paper, we expect that mantle plume heads (which may described as buoyant drops) in close spatial

Thermocapillary migration

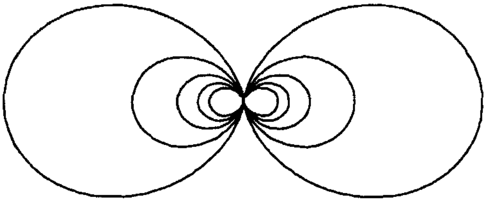

Point force

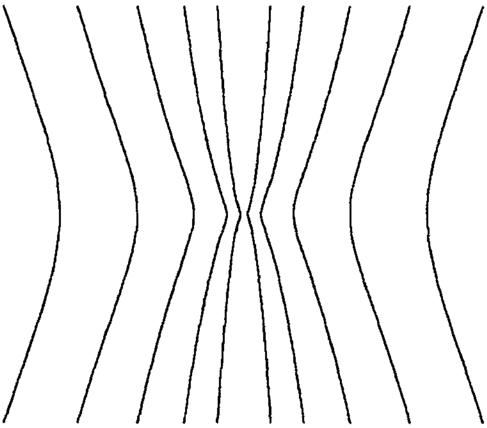

FIGURE 22. The flow produced by a small drop in thermocapillary motion, and the flow produced by a point force. Both flows produce drop deformation which may eventually lead to drop alignment.

and temporal proximity would tend to merge. Mantle plume heads form frequently enough and rise slowly enough that situations may arise in which plumes interact, particularly during the Cretaceous period when many plumes erupted on the surface of the Earth. The interaction of plumes may explain some of the apparent variation in plume size (Richards, Duncan & Courtillot 1989) and some of the variation in the size of highlands and coronae on Venus which are thought to be produced by plumes spreading beneath the planet's surface (Koch 1993).

At smaller lengthscales, geological applications associated with high Bond number dynamics include gas bubbles in magmas, where bubble radii are less than a few centimetres. The coalescence and interactions of bubbles in ascending magmas and in magma chambers may be important processes governing the style of volcanic eruptions (Jaupart & Vergniolle 1989). Characterizing the interactions between bubbles may aid in the interpretation of the distribution of bubbles in solidified volcanic flows and understanding the process of bubble formation in magmas. In addition, at small lengthscales, the rate of coalescence of drops of liquid iron during the earliest stages of the Earth's history would affect the rate of segregation of the Earth's core and also the amount of iron and other heavy metals that were removed from the mantle (Honda, Mizutani & Yamamoto 1993). Bubbly suspensions in viscous suspending fluids also occur in a wide range of industrial processes.

Finally, we note that although we only considered buoyancy-driven drops in §§4 and 5, drop alignment should be characteristic of drops driven by other mechanisms. For example, neutrally buoyant drops driven by thermocapillary forces may also be aligned. For neutrally buoyant drops in a temperature gradient G, in which the interfacial tension gradient $\nabla\sigma \propto \boldsymbol{G}$, the external flow is described by

$$\boldsymbol{u}(\boldsymbol{r}) \propto \boldsymbol{G}\cdot\left(\frac{\boldsymbol{I}}{|\boldsymbol{r}|^3} - 3\frac{\boldsymbol{r}\,\boldsymbol{r}}{|\boldsymbol{r}|^5}\right). \tag{6.1}$$

Streamlines corresponding to (6.1) and flow due to a point force are shown in figure 22. Streamlines produced by a drop translating, as a consequence of interfacial tension variations, diverge in front of the drop and converge behind the drop. We expect deformable drops to interact similarly to the interaction shown in figures 4 and 14 (provided the trailing drop is in a region where the streamlines produced by the leading drop converge, and the leading drop is in a region where the streamlines produced by the trailing drop diverge). The magnitude of the deformation, however, will scale as $O(\mathscr{B}(a/d)^4)$ for thermocapillary flows (where the Bond number $\mathscr{B} = \mu U_c/\sigma$ is based on an average value of σ, which changes slowly as the drops translate, and the translational velocity U_c) compared to $O(\mathscr{B}(a/d)^2)$ for buoyancy-driven flows. Thus, for thermocapillary-driven motions the process of alignment will be slower than for buoyancy-driven motions since the velocity disturbances and associated deformations are weaker.

This work was supported by an NSF Presidential Young Investigator award and an ACS grant to H. A. S. and by IGPP grant #351 to R. J. O'Connell (Harvard University, Department of Earth and Planetary Sciences) and H. A. S. We acknowledge the help of Harvard undergraduates Karin Riley and Joe Rice with the experiments. Funds provided by MERCK, Chevron Corporation and the Faculty Assistance program at Harvard were used to perform the experiments. We gratefully acknowledge R. J. O'Connell for discussions and comments.

Appendix A. Integral equations for multiple fluid-interface problems

In this appendix, following the discussion in Power (1993), we derive a set of integral equations of the second kind for the interfacial velocities and bulk fluid velocities in each fluid domain in terms only of stress jumps across the bounding fluid–fluid interfaces. Previous applications of the boundary integral equations to multiple-interface problems (e.g. Stone & Leal 1990; Chi & Leal 1989) also required the solution of integral equations of the first kind for the tractions $\boldsymbol{n}\cdot\boldsymbol{T}$ on the interfaces. These earlier approaches to multiple interface problems have the disadvantage of involving the solution of numerically ill-posed integral equations of the first kind, as well as solving for twice as many unknowns as is necessary.

The Stokes equations recast as integral equations may be written as

$$\frac{1}{\mu}\int_S \boldsymbol{n}\cdot\boldsymbol{T}\cdot\boldsymbol{J}\,\mathrm{d}S_y + \int_S \boldsymbol{n}\cdot\boldsymbol{K}\cdot\boldsymbol{u}\,\mathrm{d}S_y = \begin{cases} \boldsymbol{u}(\boldsymbol{x}), & \boldsymbol{x} \text{ inside } S & \text{(A 1)}\\ \tfrac{1}{2}\boldsymbol{u}(\boldsymbol{x}), & \boldsymbol{x} = \boldsymbol{x}_s \text{ on } S & \text{(A 2)}\\ 0, & \boldsymbol{x} \text{ outside } S, & \text{(A 3)} \end{cases}$$

where S represents all surfaces bounding the fluid domain including the surface at infinity, and y is the integration variable. $\boldsymbol{J}$ and $\boldsymbol{K}$ are the known Green's functions for the velocity and stress fields, respectively, given for a three-dimensional geometry by

$$\boldsymbol{J}(\boldsymbol{r}) = \frac{1}{8\pi}\left(\frac{\boldsymbol{I}}{|\boldsymbol{r}|} + \frac{\boldsymbol{rr}}{|\boldsymbol{r}|^3}\right) \quad\text{and}\quad \boldsymbol{K}(\boldsymbol{r}) = -\frac{3}{4\pi}\frac{\boldsymbol{rrr}}{|\boldsymbol{r}|^5}, \tag{A 4}$$

where $\boldsymbol{r} = \boldsymbol{x} - \boldsymbol{y}$. Equations (A1)–(A3) follow from an application of the Reciprocal

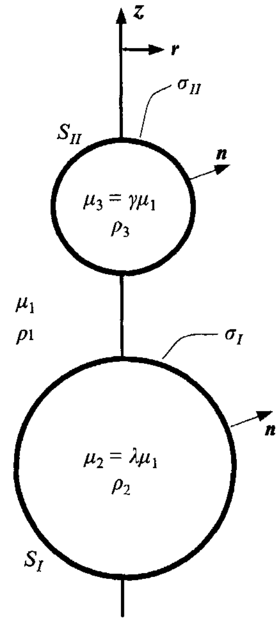

FIGURE 23. Geometry of the generic axisymmetric two-drop problem. The unit normal vector $\boldsymbol{n}$ is directed into fluid 1. Fluid viscosities are denoted by μ and fluid densities by ρ, and σ is the coefficient of interfacial tension. The surfaces of the drops are denoted by S_I and S_{II}.

theorem (for a derivation of (A1)–(A3) the reader is referred to Rallison & Acrivos 1978).

Consider the case of two fluid drops, with volumes V_2 and V_3, in an unbounded fluid of volume V_1 (figure 23). We can neglect bounding surfaces at large distances since disturbance Stokes flow fields decay as $O(r^{-1})$ and stresses decay as $O(r^{-2})$. As in § 2 we require that velocities be continuous across fluid interfaces. For the problem shown in figure 23 the stress jumps are given by

$$[\![\boldsymbol{n}\cdot\boldsymbol{T}^I]\!] = \boldsymbol{n}\cdot\boldsymbol{T}_1^I - \boldsymbol{n}\cdot\boldsymbol{T}_2^I = \sigma_I\,(\nabla_s\cdot\boldsymbol{n})\boldsymbol{n} - \nabla_s\sigma_I - \boldsymbol{n}(\rho_2-\rho_1)\boldsymbol{g}\cdot\boldsymbol{x} \quad \text{on } S_I, \tag{A 5}$$

$$[\![\boldsymbol{n}\cdot\boldsymbol{T}^{II}]\!] = \boldsymbol{n}\cdot\boldsymbol{T}_1^{II} - \boldsymbol{n}\cdot\boldsymbol{T}_3^{II} = \sigma_{II}\,(\nabla_s\cdot\boldsymbol{n})\boldsymbol{n} - \nabla_s\sigma_{II} - \boldsymbol{n}(\rho_3-\rho_1)\boldsymbol{g}\cdot\boldsymbol{x} \quad \text{on } S_{II}. \tag{A 6}$$

For each fluid domain, we can write the set of equations

$$-\frac{1}{\mu_2}\int_{S_I}\boldsymbol{n}\cdot\boldsymbol{T}_2\cdot\boldsymbol{J}\,\mathrm{d}S_y - \int_{S_I}\boldsymbol{n}\cdot\boldsymbol{K}\cdot\boldsymbol{u}_2\,\mathrm{d}S_y = \begin{cases}\boldsymbol{u}_2(\boldsymbol{x}), & \boldsymbol{x}\in V_2 \notin V_1, V_3\\ \tfrac{1}{2}\boldsymbol{u}_2(\boldsymbol{x}_s), & \boldsymbol{x}_s\in S_I\\ 0, & \boldsymbol{x}\notin V_2,\end{cases} \tag{A 7}$$

$$-\frac{1}{\mu_3}\int_{S_{II}}\boldsymbol{n}\cdot\boldsymbol{T}_3\cdot\boldsymbol{J}\,\mathrm{d}S_y - \int_{S_{II}}\boldsymbol{n}\cdot\boldsymbol{K}\cdot\boldsymbol{u}_3\,\mathrm{d}S_y = \begin{cases}\boldsymbol{u}_3(\boldsymbol{x}), & \boldsymbol{x}\in V_3 \notin V_1, V_2\\ \tfrac{1}{2}\boldsymbol{u}_3(\boldsymbol{x}_s), & \boldsymbol{x}_s\in S_{II}\\ 0, & \boldsymbol{x}\notin V_3,\end{cases} \tag{A 8}$$

and

$$\frac{1}{\mu_1}\int_{S_I} \boldsymbol{n}\cdot\boldsymbol{T}_1\cdot\boldsymbol{J}\mathrm{d}S_y + \int_{S_I} \boldsymbol{n}\cdot\boldsymbol{K}\cdot\boldsymbol{u}_1\,\mathrm{d}S_y$$
$$+\frac{1}{\mu_1}\int_{S_{II}} \boldsymbol{n}\cdot\boldsymbol{T}_1\cdot\boldsymbol{J}\,\mathrm{d}S_y + \int_{S_{II}} \boldsymbol{n}\cdot\boldsymbol{K}\cdot\boldsymbol{u}_1\,\mathrm{d}S_y = \begin{cases} \boldsymbol{u}_1(\boldsymbol{x}), & \boldsymbol{x}\in V_1 \notin V_2, V_3 \\ 0, & \boldsymbol{x}\in V_2, V_3 \\ \frac{1}{2}\boldsymbol{u}_1(\boldsymbol{x}), & \boldsymbol{x}_s \in S_I, S_{II}, \end{cases} \tag{A 9}$$

where $\boldsymbol{n}$ is the unit inward normal from fluid 1, as shown in figures 2 and 23. Multiplying (A7) by λ (the viscosity ratio between fluids 1 and 2) and adding to (A9), multiplying (A8) by γ (the viscosity ratio between fluids 1 and 3) and adding to (A9) and using the stress boundary conditions (A5)–(A6), we obtain a system of coupled integral equations for the interfacial velocities, which may written compactly as

$$-\frac{1}{\mu_1}\int_{S_I} [\![\boldsymbol{n}\cdot\boldsymbol{T}^I]\!]\cdot\boldsymbol{J}\mathrm{d}S_y - (1-\lambda)\int_{S_I} \boldsymbol{n}\cdot\boldsymbol{K}\cdot\boldsymbol{u}^I\mathrm{d}S_y - \frac{1}{\mu_1}\int_{S_{II}} [\![\boldsymbol{n}\cdot\boldsymbol{T}^{II}]\!]\cdot\boldsymbol{J}\mathrm{d}S_y$$
$$-(1-\gamma)\int_{S_{II}} \boldsymbol{n}\cdot\boldsymbol{K}\cdot\boldsymbol{u}^{II}\mathrm{d}S_y = \begin{cases} \boldsymbol{u}_1(\boldsymbol{x}), & \boldsymbol{x}\in V_1 & \text{(A 10}a\text{)} \\ \lambda\boldsymbol{u}_2(\boldsymbol{x}), & \boldsymbol{x}\in V_2 & \text{(A 10}b\text{)} \\ \gamma\boldsymbol{u}_3(\boldsymbol{x}), & \boldsymbol{x}\in V_3 & \text{(A 10}c\text{)} \\ \dfrac{1+\lambda}{2}\boldsymbol{u}^I(\boldsymbol{x}_s), & \boldsymbol{x}_s\in S_I & \text{(A 10}d\text{)} \\ \dfrac{1+\gamma}{2}\boldsymbol{u}^{II}(\boldsymbol{x}_s), & \boldsymbol{x}_s\in S_{II}. & \text{(A 10}e\text{)} \end{cases}$$

To calculate the interfacial velocities $\boldsymbol{u}^I$ and $\boldsymbol{u}^{II}$ we solve equations (A10*d,e*) which are coupled integral equations of the second kind. Once the interfacial velocities are known, the velocities in the drop and bulk fluid may be calculated from (A10*a–c*).

Appendix B. Stokes flow kernels in two dimensions

For a two-dimensional point force at $\boldsymbol{y}$, the fundamental singular solutions (kernels) $\boldsymbol{J}^{sing}$ and $\boldsymbol{K}^{sing}$ which appear in (2.8) are given, respectively, by

$$\boldsymbol{J}^{sing}(\boldsymbol{r}) = \frac{1}{4\pi}\left(\boldsymbol{I}\log|\boldsymbol{r}| - \frac{\boldsymbol{rr}}{|\boldsymbol{r}|^2}\right) \tag{B 1}$$

and

$$\boldsymbol{K}^{sing}(\boldsymbol{r}) = \frac{1}{\pi}\frac{\boldsymbol{rrr}}{|\boldsymbol{r}|^4}, \tag{B 2}$$

where $\boldsymbol{r} = \boldsymbol{x} - \boldsymbol{y}$, and $\boldsymbol{x}$ is the point at which velocity is to be calculated.

For flow reflectionally symmetric across a plane at $z = h$ (free-slip and zero vertical velocity boundary conditions apply along this plane), the fundamental singular solution for $\boldsymbol{J}$ (with a similar solution for $\boldsymbol{K}$) is given by

$$J_{ij}(\boldsymbol{r}) = J_{ij}^{sing}(\boldsymbol{r}) + (-1)^{j+1}J_{ij}^{sing}(\tilde{\boldsymbol{r}}), \tag{B 3}$$

where $\tilde{\boldsymbol{r}} = \boldsymbol{r} - 2h\boldsymbol{e}_z$, and the indices $i, j = 1, 2$ correspond to the x- and z-directions, respectively (Pozrikidis 1992*b*). The inclusion of an image Stokeslet resolves Stokes paradox since the logarithmic singularity in the velocity kernel (B1) disappears. The function $\boldsymbol{J}$ given by (B3) is the appropriate image system kernel to use in the integral equation (2.8) for a two-dimensional geometry with a planar free-slip surface.

Appendix C. The reciprocal theorem applied to the translation of non-spherical drops

C.1. *Perturbation solution for the translation of a non-spherical drop*

The non-dimensionalized Stokes flow boundary value problem for a deformed drop with radius

$$r = 1 + \epsilon f(\theta, \phi)$$

has the form

$$\left. \begin{array}{llll} \nabla \cdot \boldsymbol{T} = 0, & r > 1 + \epsilon f(\theta,\phi), & \nabla \cdot \hat{\boldsymbol{T}} = 0, & r < 1 + \epsilon f(\theta,\phi) \\ \nabla \cdot \boldsymbol{u} = 0, & & \nabla \cdot \hat{\boldsymbol{u}} = 0; & \end{array} \right\} \qquad (\text{C}\,1)$$

with boundary conditions

$$\boldsymbol{u} - \hat{\boldsymbol{u}} = 0 \ \text{ on } \ S, \qquad (\text{C}\,2)$$

$$\boldsymbol{u} \cdot \boldsymbol{n} = \boldsymbol{U} \cdot \boldsymbol{n} \ \text{ on } \ S, \qquad (\text{C}\,3)$$

$$\boldsymbol{n} \cdot \boldsymbol{T} - \lambda \boldsymbol{n} \cdot \hat{\boldsymbol{T}} = \frac{3(2+3\lambda)}{2\mathscr{B}(1+\lambda)} \boldsymbol{n} \nabla_s \cdot \boldsymbol{n} + \frac{3(2+3\lambda)}{2(1+\lambda)} \hat{\boldsymbol{g}} \cdot \boldsymbol{x} \boldsymbol{n} \ \text{ on } \ S, \qquad (\text{C}\,4)$$

where S is the deformed drop shape, $\boldsymbol{U}$ is the steady translational velocity of the drop, and $\hat{\boldsymbol{g}}$ is a unit vector in the direction of the gravitational acceleration. Velocities are normalized by the Hadamard–Rybzcyński velocity $U^{(0)}$ given by equation (5.1). Lengths are normalized by the drop radius a, and the stress and pressure are normalized by $\mu U/a$ and $\lambda \mu U/a$ outside and inside the drop, respectively. The parameter ϵ is small, $\epsilon \ll 1$. It follows that the normal and the curvature of nearly spherical surfaces, may be expanded as

$$\boldsymbol{n} = \boldsymbol{n}_o - \epsilon \nabla_e f + O(\epsilon^2) \qquad (\text{C}\,5)$$

and

$$\nabla_s \cdot \boldsymbol{n} = 2 - \epsilon[\nabla_e^2 f + 2f] + O(\epsilon^2), \qquad (\text{C}\,6)$$

where $\boldsymbol{n}_o$ is a unit normal to the spherical surface and $\nabla_e = (\boldsymbol{I} - \boldsymbol{n}_o \boldsymbol{n}_o) \cdot \nabla$ is the surface gradient operator measuring variations along the spherical surface. The shape function $f(\theta, \phi)$ in spherical polar coordinates (defined in figure 19 and calculated in § 5.3) has the form

$$f = \frac{(2+3\lambda)(16+19\lambda)}{48(1+\lambda)^2} \cos\beta \left(1 - 3\cos^2\theta\right). \qquad (\text{C}\,7)$$

It follows that

$$\nabla_e f = \frac{(2+3\lambda)(16+19\lambda)}{8(1+\lambda)^2} \cos\beta \cos\theta \sin\theta \ \boldsymbol{e}_\theta, \qquad (\text{C}\,8)$$

where $\boldsymbol{e}_\theta$ is a unit vector in the θ-direction, and

$$\nabla_e^2 f = \frac{(2+3\lambda)(16+19\lambda)}{8(1+\lambda)^2} \cos\beta \left(3\cos^2\theta - 1\right). \qquad (\text{C}\,9)$$

To use the Reciprocal theorem we need to apply the boundary conditions (C2)–(C4) on a spherical surface. First we introduce the expansion for $\boldsymbol{u}(\boldsymbol{x})$ analogous to the expansion for $\boldsymbol{U}$ given by (5.17) (with a similar expression for $\boldsymbol{T}(\boldsymbol{x})$):

$$\boldsymbol{u}(\boldsymbol{x}) = \boldsymbol{u}^{(0)}(\boldsymbol{x}) + \left(\frac{a}{d}\right) \boldsymbol{u}^{(1)}(\boldsymbol{x}) + \mathscr{B} \left(\frac{a}{d}\right)^2 \boldsymbol{u}^{(2)}(\boldsymbol{x}) + O\left(u^{(0)} \frac{a^3}{d^3}\right). \qquad (\text{C}\,10)$$

We can expand $\boldsymbol{u}$ in a Taylor series in the neighbourhood of a spherical surface:

$$\begin{aligned}\boldsymbol{u}(r=1+\epsilon f) &= \boldsymbol{u}|_{r=1} + \epsilon f \frac{\partial \boldsymbol{u}}{\partial r}\Big|_{r=1} + \frac{1}{2}(\epsilon f)^2 \frac{\partial^2 \boldsymbol{u}}{\partial r^2}\Big|_{r=1} \\ &= \boldsymbol{u}^{(0)}|_{r=1} + \mathscr{B}\left(\frac{a}{d}\right)^2 \left[\boldsymbol{u}^{(2)} + f\frac{\partial \boldsymbol{u}^{(0)}}{\partial r}\right]_{r=1} + \cdots \qquad \text{(C 11)}\end{aligned}$$

The $O(a/d)$ problem corresponds to a spherical drop translating with velocity $\boldsymbol{U}^{(1)}$ given in (5.8) and thus does not appear at $O(\mathscr{B}a^2/d^2)$. The continuity of velocity boundary condition (C2) for the $O(\epsilon)$ terms leads to

$$\begin{aligned}\boldsymbol{u}^{(2)} - \hat{\boldsymbol{u}}^{(2)} &= -f\left[\frac{\partial \boldsymbol{u}^{(0)}}{\partial r} - \frac{\partial \hat{\boldsymbol{u}}^{(0)}}{\partial r}\right] \qquad \text{(C 12)} \\ &= f\frac{3(\lambda-1)\boldsymbol{U}^{(0)}}{2(1+\lambda)} \cdot [\boldsymbol{I} - \boldsymbol{n}_o\boldsymbol{n}_o] \quad \text{at} \quad r=1. \qquad \text{(C 13)}\end{aligned}$$

The $O(\epsilon)$ contribution to the normal velocity boundary condition (C3) gives

$$\begin{aligned}\boldsymbol{u}^{(2)} \cdot \boldsymbol{n}_o &= \boldsymbol{u}^{(0)} \cdot \nabla_e f - f\boldsymbol{n}_o \cdot \frac{\partial \boldsymbol{u}^{(0)}}{\partial r} - \boldsymbol{U}^{(0)} \cdot \nabla_e f + \boldsymbol{U}^{(2)} \cdot \boldsymbol{n}_o \qquad \text{(C 14)} \\ &= f\frac{\boldsymbol{U}^{(0)} \cdot \boldsymbol{n}_o}{1+\lambda} - \frac{\boldsymbol{U}^{(0)} \cdot \nabla_e f}{2(1+\lambda)} + \boldsymbol{U}^{(2)} \cdot \boldsymbol{n}_o \quad \text{at} \quad r=1. \qquad \text{(C 15)}\end{aligned}$$

Similarly, we expand the stress in a Taylor series:

$$\begin{aligned}\boldsymbol{T}(r=1+\epsilon f) &= \boldsymbol{T}|_{r=1} + \epsilon f \frac{\partial \boldsymbol{T}}{\partial r}\Big|_{r=1} + \frac{1}{2}(\epsilon f)^2 \frac{\partial^2 \boldsymbol{T}}{\partial r^2}\Big|_{r=1} + \cdots \\ &= \boldsymbol{T}^{(0)}|_{r=1} + \mathscr{B}\left(\frac{a}{d}\right)^2 \left[\boldsymbol{T}^{(2)} + f\frac{\partial \boldsymbol{T}^{(0)}}{\partial r}\right]_{r=1} + \cdots. \qquad \text{(C 16)}\end{aligned}$$

On the spherical surface, the $O(\epsilon)$ stress boundary condition (C4) becomes

$$\begin{aligned}\boldsymbol{n}_o \cdot \boldsymbol{T}^{(2)} - \lambda\boldsymbol{n}_o \cdot \hat{\boldsymbol{T}}^{(2)} &= -f\frac{\partial}{\partial r}\left[\boldsymbol{n}_o \cdot \boldsymbol{T}^{(0)} - \lambda\boldsymbol{n}_o \cdot \hat{\boldsymbol{T}}^{(0)}\right] + \nabla_e f \cdot \left(\boldsymbol{T}^{(0)} - \lambda\hat{\boldsymbol{T}}^{(0)}\right) \\ &\quad - \frac{3(2+3\lambda)}{2\mathscr{B}(1+\lambda)}\left[2\nabla_e f + \boldsymbol{n}_o\left(\nabla_e^2 f + 2f\right)\right] \\ &\quad + \frac{3(2+3\lambda)}{2(1+\lambda)}\left[f(\hat{\boldsymbol{g}} \cdot \boldsymbol{n}_o)\boldsymbol{n}_o - (\boldsymbol{g} \cdot \boldsymbol{n}_o)\nabla_e f\right] \qquad \text{(C 17)} \\ &= -f\frac{3\boldsymbol{U}^{(0)}}{2(1+\lambda)} \cdot (5\lambda\boldsymbol{I} + (4-9\lambda)\boldsymbol{n}_o\boldsymbol{n}_o) - 15\frac{\boldsymbol{U}^{(0)} \cdot \boldsymbol{n}_o}{2(1+\lambda)}\nabla_e f \\ &\quad - \frac{3(2+3\lambda)}{2\mathscr{B}(1+\lambda)}\boldsymbol{n}_o\left[\nabla_e^2 f + 2\boldsymbol{n}_o f\right] \\ &\quad + \frac{3(2+3\lambda)}{2(1+\lambda)}\left[f(\hat{\boldsymbol{g}} \cdot \boldsymbol{n}_o)\boldsymbol{n}_o - (\boldsymbol{g} \cdot \boldsymbol{n}_o)\nabla_e f\right] \quad \text{at} \quad r=1. \qquad \text{(C 18)}\end{aligned}$$

The boundary value problem for $\boldsymbol{u}^{(2)}$ may now be set up for a spherical geometry:

$$\begin{aligned}&\nabla \cdot \boldsymbol{T}^{(2)} = 0, \quad r>1, \qquad \nabla \cdot \hat{\boldsymbol{T}}^{(2)} = 0, \quad r<1, \\ &\nabla \cdot \boldsymbol{u}^{(2)} = 0, \qquad\qquad\quad \nabla \cdot \hat{\boldsymbol{u}}^{(2)} = 0; \qquad \text{(C 19)}\end{aligned}$$

$$\boldsymbol{u}^{(2)} - \hat{\boldsymbol{u}}^{(2)} = \boldsymbol{A}(\boldsymbol{n}_o, f) \quad \text{on} \quad r=1, \qquad \text{(C 20)}$$

$$\boldsymbol{u}^{(2)} \cdot \boldsymbol{n}_o = B(\boldsymbol{n}_o, f) + \boldsymbol{U}^{(2)} \cdot \boldsymbol{n}_o \quad \text{on} \quad r=1, \qquad \text{(C 21)}$$

$$\boldsymbol{n}_o \cdot \boldsymbol{T}^{(2)} - \lambda \boldsymbol{n}_o \cdot \hat{\boldsymbol{T}}^{(2)} = \boldsymbol{C}(\boldsymbol{n}_o, f) \quad \text{on} \quad r = 1, \tag{C 22}$$

where the vector and scalar functions $\boldsymbol{A}$, $\boldsymbol{C}$ and B are given in equations (C13), (C18) and (C15). $\boldsymbol{A}$, $\boldsymbol{C}$ and B are functions of position defined on a spherical surface S involving the Hadamard–Rybzcyński velocity field and the first approximation to the drop shape $f(\theta, \phi)$. Using the Reciprocal theorem, as outlined in Haj-Hariri *et al.* (1990), we can determine the second-order correction to the rise speed of the deformed drop $\boldsymbol{U}^{(2)}$ without solving for the detailed flow field $\boldsymbol{u}^{(2)}(\boldsymbol{x})$.

C.2. *Application of the Reciprocal theorem*

Consider the complementary flow problem for a spherical drop translating with velocity $\boldsymbol{U}^*$, non-dimensionalized as in § C.1:

$$\left.\begin{array}{llll} \nabla \cdot \boldsymbol{T}^* = 0, & r > 1 & \nabla \cdot \hat{\boldsymbol{T}}^* = 0, & r < 1, \\ \nabla \cdot \boldsymbol{u}^* = 0, & & \nabla \cdot \hat{\boldsymbol{u}}^* = 0; & \end{array}\right\} \tag{C 23}$$

$$\boldsymbol{u}^* - \hat{\boldsymbol{u}}^* = 0 \quad \text{on} \quad r = 1, \tag{C 24}$$

$$\boldsymbol{u}^* \cdot \boldsymbol{n}_o = \hat{\boldsymbol{u}}^* \cdot \boldsymbol{n}_o = \boldsymbol{U}^* \cdot \boldsymbol{n}_o \quad \text{on} \quad r = 1, \tag{C 25}$$

$$\boldsymbol{t} \cdot \left[\boldsymbol{n}_o \cdot \boldsymbol{T}^* - \lambda \boldsymbol{n}_o \cdot \hat{\boldsymbol{T}}^*\right] = 0 \quad \text{on} \quad r = 1. \tag{C 26}$$

Here $\boldsymbol{t}$ is a unit vector tangent to the spherical surface S.

For Stokes flows, we make use of the identities

$$\nabla \cdot \left(\boldsymbol{T}^* \cdot \boldsymbol{u}^{(2)}\right) = \nabla \cdot \left(\boldsymbol{T}^{(2)} \cdot \boldsymbol{u}^*\right) \quad \text{and} \quad \nabla \cdot \left(\hat{\boldsymbol{T}}^* \cdot \hat{\boldsymbol{u}}^{(2)}\right) = \nabla \cdot \left(\hat{\boldsymbol{T}}^{(2)} \cdot \hat{\boldsymbol{u}}^*\right) \tag{C 27}$$

and the divergence theorem to derive the pair of integral relations

$$\int_S \boldsymbol{n}_o \cdot \boldsymbol{T}^{(2)} \cdot \boldsymbol{u}^* \mathrm{d}S = \int_S \boldsymbol{n}_o \cdot \boldsymbol{T}^* \cdot \boldsymbol{u}^{(2)} \mathrm{d}S \tag{C 28}$$

$$\int_S \boldsymbol{n}_o \cdot \hat{\boldsymbol{T}}^{(2)} \cdot \hat{\boldsymbol{u}}^* \mathrm{d}S = \int_S \boldsymbol{n}_o \cdot \hat{\boldsymbol{T}}^* \cdot \hat{\boldsymbol{u}}^{(2)} \mathrm{d}S \tag{C 29}$$

where integrals over bounding surfaces at large distances vanish owing to the sufficiently rapid decay of the integrands. Subtracting λ times (C29) from (C28) gives

$$\int_S \left[\boldsymbol{n}_o \cdot \boldsymbol{T}^{(2)} - \lambda \boldsymbol{n}_o \cdot \hat{\boldsymbol{T}}^{(2)}\right] \cdot \boldsymbol{u}^* \mathrm{d}S = \int_S \left[\boldsymbol{n}_o \cdot \boldsymbol{T}^* \cdot \boldsymbol{u}^{(2)} - \lambda \boldsymbol{n}_o \cdot \hat{\boldsymbol{T}}^* \cdot \hat{\boldsymbol{u}}^{(2)}\right] \mathrm{d}S, \tag{C 30}$$

where we have made use of boundary condition (C24), $\boldsymbol{u}^* = \hat{\boldsymbol{u}}^*$ on S.

The solution to the complementary problem (C23)–(C26) for $\boldsymbol{u}^*$, $\boldsymbol{T}^*$, $\hat{\boldsymbol{u}}^*$ and $\hat{\boldsymbol{T}}^*$ is straightforward, and is given by

$$\boldsymbol{u}^*(\boldsymbol{r}) = \frac{\lambda}{4(1+\lambda)} \left[\frac{\boldsymbol{U}^*}{r^3} - 3\frac{\boldsymbol{U}^* \cdot \boldsymbol{rr}}{r^5}\right] + \frac{2+3\lambda}{4(1+\lambda)} \left[\frac{\boldsymbol{U}^*}{r} + \frac{\boldsymbol{U}^* \cdot \boldsymbol{rr}}{r^3}\right], \tag{C 31}$$

$$\hat{\boldsymbol{u}}^*(\boldsymbol{r}) = \frac{3+2\lambda}{2(1+\lambda)} \boldsymbol{U}^* - \frac{1}{2(1+\lambda)} \left[2r^2 \boldsymbol{U}^* - \boldsymbol{U}^* \cdot \boldsymbol{rr}\right], \tag{C 32}$$

$$\begin{aligned} \boldsymbol{T}^*(\boldsymbol{r}) = -p_\infty \boldsymbol{I} - \frac{\lambda}{2(1+\lambda)} & \left[3\frac{\boldsymbol{U}^*\boldsymbol{r} + \boldsymbol{r}\boldsymbol{U}^* + \boldsymbol{r} \cdot \boldsymbol{U}^*\boldsymbol{I}}{r^5} - 15\frac{\boldsymbol{U}^* \cdot \boldsymbol{rrr}}{r^7}\right] \\ & - \frac{3(2+3\lambda)}{2(1+\lambda)} \frac{\boldsymbol{U}^* \cdot \boldsymbol{rrr}}{r^5}, \end{aligned} \tag{C 33}$$

$$\hat{\boldsymbol{T}}^*(\boldsymbol{r}) = -\lambda p_o \boldsymbol{I} + \frac{1}{2(1+\lambda)} \left[12\boldsymbol{U}^* \cdot \boldsymbol{r}\boldsymbol{I} - 3(\boldsymbol{U}^*\boldsymbol{r} + \boldsymbol{r}\boldsymbol{U}^*)\right]. \tag{C 34}$$

Here p_o and p_∞ are constant pressures inside and outside the drop, respectively.

Thus, for the second-order velocity correction we arrive at

$$\boldsymbol{U}^{(2)} = -\frac{1}{4\pi(2+3\lambda)} \int_S \{[(1+2\lambda)\boldsymbol{I} + \boldsymbol{n}_o\boldsymbol{n}_o]\cdot \boldsymbol{C}(\boldsymbol{n}_o, f) + 3\lambda\,[\boldsymbol{I} - 3\boldsymbol{n}_o\boldsymbol{n}_o]\cdot \boldsymbol{A}(\boldsymbol{n}_o, f) \\ + 3(2+3\lambda)B(\boldsymbol{n}_o, f)\boldsymbol{n}_o\}\,\mathrm{d}S. \qquad \text{(C 35)}$$

The detailed equations presented here differ slightly from those in Haj-Hariri *et al.* (1990) because of a different choice of reference frame.

REFERENCES

Acrivos, A. 1983 The breakup of small drops and bubbles in shear flows. *4th Intl Conf. on Physicochemical Hydrodynamics, Ann. N.Y. Acad. Sci.* **404**, 1–11.

Barnocky, G. & Davis, R.H. 1989 The lubrication force between spherical drops, bubbles and rigid particles in a viscous fluid. *Intl J. Multiphase Flow* **15**, 627–638.

Batchelor, G.K. 1967 *An Introduction to Fluid Dynamics*. Cambridge University Press.

Boor, C. de 1978 *A Practical Guide to Splines*. Springer.

Bruijn, R.A. de 1989 Deformation and breakup of drops in simple shear flows. PhD thesis, Technical University at Eindhoven.

Chi, B.K. & Leal, L.G. 1989 A theoretical study of the motion of a viscous drop toward a fluid interface at low Reynolds number. *J. Fluid Mech.* **201**, 123–146.

Davis, R.H., Schonberg, J.A. & Rallison, J.M. 1989 The lubrication force between two viscous drops. *Phys. Fluids* A **1**, 77–81.

Griffiths, R.W. & Campbell, I.H. 1990 Stirring and structure in mantle starting plumes. *Earth Planet. Sci. Lett.* **99**, 66–78.

Griffiths, R.W., Gurnis, M. & Eitelberg, G. 1989 Holographic measurements of surface topography in laboratory models of mantle hotspots. *Geophys. J.* **96**, 477–495.

Haber, S., Hetsroni, G. & Solan, A. 1973 Low Reynolds number motion of two drops submerged in an unbounded arbitrary velocity field. *Intl J. Multiphase Flow* **4**, 627–638.

Haj-Hariri, H., Nadim, A. & Borhan, A. 1990 Effect of inertia on the thermocapillary velocity of a drop. *J. Colloid Interface Sci.* **140**, 277–286.

Happel, J. & Brenner, H. 1965 *Low Reynolds Number Hydrodynamics*. Prentice-Hall.

Honda, R., Mizutani, H. & Yamamoto, T. 1993 Numerical simulations of Earth's core formation. *J. Geophys. Res.* **98**, 2075–2089.

Jaupart, C. & Vergniolle, S. 1989 The generation and collapse of a foam layer at the roof of a basaltic magma chamber. *J. Fluid Mech.* **203**, 347–380.

Jeong, J.-T. & Moffatt, H.K. 1992 Free-surface cusps associated with flow at low Reynolds number. *J. Fluid Mech.* **241**, 1–22.

Joseph, D.D., Nelson, J., Renardy, M. & Renardy Y. 1991 Two-dimensional cusped interfaces. *J. Fluid Mech.* **223**, 383–409.

Kim, S. & Karrila, S.J. 1991 *Microhydrodynamics: Principles and Selected Applications*. Butterworth-Heineman.

Koch, D.L. & Shaqfeh, E.S.G. 1989 The instability of a dispersion of sedimenting spheroids. *J. Fluid Mech.* **209**, 521–542.

Koch, D.M. 1993 A spreading drop model for mantle plumes and volcanic features on Venus. PhD thesis, Yale University.

Koh, C.J. & Leal, L.G. 1989 The stability of drop shapes for translation at zero Reynolds number through a quiescent fluid. *Phys. Fluids* A **1**, 1309–1313.

Kojima, M., Hinch, E. J. & Acrivos, A. 1984 The formation and expansion of a toroidal drop moving in a viscous fluid. *Phys. Fluids* **27**, 19–32.

Leal, L. G. 1992 *Laminar Flow and Convective Transport Processes*. Butterworth-Heineman.

Lee, S. H. & Leal, L. G. 1982 The motion of a sphere in the presence of a deformable interface. II. A numerical study of the translation of a sphere normal to an interface. *J. Colloid Interface Sci.* **87**, 81–106.

MANGA, M., STONE, H. A. & O'CONNELL, R. J. 1993 The interaction of plume heads with compositional discontinuities in the Earth's mantle. *J. Geophys. Res.*, in press.

NEWHOUSE, L. A. & POZRIKIDIS, C. 1990 The Rayleigh–Taylor instability of a viscous liquid layer resting on a plane wall. *J. Fluid Mech.* **217**, 615–638.

OLSON, P. & SINGER, H. 1985 Creeping plumes. *J. Fluid Mech.* **158**, 511–531.

POWER, H. 1993 Low Reynolds number deformation of compound drops in shear flow. *Math. Meth. Appl Sci.* **16**, 61-74.

POZRIKIDIS, C. 1990 The instability of a moving viscous drop. *J. Fluid Mech.* **210**, 1-21.

POZRIKIDIS, C. 1992*a* The buoyancy-driven motion of a train of viscous drops within a cylindrical tube. *J. Fluid Mech.* **237**, 627–648.

POZRIKIDIS, C. 1992*b* *Boundary Integral and Singularity Methods for Linearized Viscous Flow.* Cambridge University Press.

RALLISON, J. M. & ACRIVOS, A. 1978 A numerical study of the deformation and burst of a viscous drop in an extensional flow. *J. Fluid Mech.* **89**, 191–200.

RICHARDS, M. A., DUNCAN, R. A. & COURTILLOT, V. E. 1989 Flood basalts and hotspot tracks: Plume heads and tails. *Science* **246**, 103–107.

STONE, H. A. & LEAL, L. G. 1989 Relaxation and breakup of an initially extended drop in an otherwise quiescent fluid. *J. Fluid Mech.* **198**, 399–427.

STONE, H. A. & LEAL, L. G. 1990 Breakup of concentric double emulsion droplets in linear flows. *J. Fluid Mech.* **211**, 123–156.

TANZOSH, J., MANGA, M. & STONE, H. A. 1992 Boundary element methods for viscous free-surface flow problems: Deformation of single and multiple fluid-fluid interfaces. In *Boundary Element Technolgies* (ed. C. A. Brebbia & M. S. Ingber), pp. 19–39. Computational Mechanics Publications and Elsevier Applied Science, Southampton.

TAYLOR, G. I. 1932 The viscosity of a fluid containing small drops of another fluid. *Proc. R. Soc. Lond.* A **138**, 41–48.

UNVERDI, S. O. & TRYGGVASON, G. 1992 A front-tracking method for viscous, incompressible, multi-fluid flows. *J. Comput. Phys.* **100**, 25–37.

YIANTSIOS, S. G. & DAVIS, R. H. 1990 On the buoyancy-driven motion of a drop towards a rigid or deformable interface. *J. Fluid Mech.* **217**, 547–573.

YIANTSIOS, S. G. & DAVIS, R. H. 1991 Close approach and deformation of two viscous drops due to gravity and van der Waals forces. *J. Colloid Interface Sci.* **144**, 412–433.